

# Variability in the timing of a $\beta$ -catenin pulse biases a stochastic cell fate decision in *C. elegans*

Jason R. Kroll, Jasonas Tsiaxiras, and Jeroen S. van Zon<sup>1</sup>

AMOLF  
Science Park 104  
1098 XG, Amsterdam  
The Netherlands

## Summary

During development, cell fate decisions are often highly stochastic, but with the frequency of the different possible fates tightly controlled. To understand how signaling networks control the cell fate frequency of such random decisions, we studied the stochastic differentiation of the *C. elegans* P3.p cell, using time-lapse microscopy to measure the single-cell dynamics of key regulators of cell fate frequency. Strikingly, we observed pulsatile accumulation dynamics of BAR-1/ $\beta$ -catenin, a key component in Wnt signaling, during the cell fate decision. Combining quantitative analysis and mathematical modeling, we found that the timing of the BAR-1/ $\beta$ -catenin pulse was a key determinant of the outcome of the cell fate decision. Our results highlight that timing of cell signaling dynamics, rather than its average level or amplitude, can play an instructive role in determining cell fate.

## Keywords

cell fate; *C. elegans*; stochastic dynamics; single-cell dynamics; Wnt signaling; beta-catenin; pulses

---

<sup>1</sup> Lead contact (J.v.Zon@amolf.nl)

# Introduction

During development, cells robustly obtain the correct cell fate to give rise to a viable adult organism, despite internal molecular noise and environmental variability. It is commonly assumed that suppressing this variability is essential for successful development. However, stochastic cell fate decisions, where cells randomly assume one cell fate out of a limited repertoire of different fates, is the cornerstone of many developmental processes (Johnston and Desplan 2010). For example, the first cell fate decision in the mouse embryo, between trophoderm or primitive endoderm fate, is stochastic (Zernicka-Goetz *et al.* 2009). Similarly, photoreceptor cells in the human retina randomly express either a red, green or blue photoreceptor gene (Roorda and Williams 1999; Smallwood *et al.* 2002). In these stochastic decision processes, even though each individual outcome is random, the relative frequency of the different cells fates is often tightly controlled.

Currently, stochastic cell fate decisions are best understood in the context of single-celled organisms, where gene expression noise dominates as the key source of variability driving stochastic cell fate decisions (Balaban 2004; Süel *et al.* 2006; Maamar *et al.* 2007; Losick and Desplan 2008). However, it remains poorly understood how stochastic cell fate decisions are regulated during animal development, as multicellular organisms pose unique constraints compared to single-celled organisms. Here, stochastic cell fate decisions have to be precisely coordinated with developmental timing, are potentially influenced by neighboring cells and rely on external, long-range signals mediated by a small number of key developmental signaling pathways. How these canonical signaling pathways drive stochastic cell fate decisions with strong control over cell fate frequencies is an open question.

The Wnt pathway is a highly conserved signaling pathway that regulates many developmental events and cell fates (Mucenski *et al.* 2003; Hirabayashi 2004; Ohyama 2006; Clevers and Nusse 2012; Hudson *et al.* 2013; Lindström *et al.* 2014). In the canonical pathway, the presence of Wnt ligands leads to the accumulation of the transcriptional co-activator  $\beta$ -catenin, which co-regulates Wnt pathway target genes (Eisenmann *et al.* 1998; Korswagen *et al.* 2000; Korswagen 2002; Sawa and Korswagen 2013). During *C. elegans* larval development, the Wnt/ $\beta$ -catenin pathway is required for specification of vulval precursor cell (VPC) competence group early in the L2 larval stage (Gleason *et al.* 2002; Myers and Greenwald 2007). This group consists of six epidermal cells named P3.p-P8.p, which are subsequently patterned to various vulval cell fates by multiple signaling pathways (Sternberg and Horvitz 1986; Hill and Sternberg 1993; Eisenmann *et al.* 1998; Gleason *et al.* 2002; Félix 2012; Gupta *et al.* 2012).

The establishment of the VPC competence group is partly stochastic, as the P3.p cell assumes VPC fate in only ~50% of wild-type hermaphrodites (Fig. 1a). In the other 50%, P3.p assumes hypodermal fate by fusing to a neighboring syncytial hypodermal cell, called hyp7 (Sternberg and Horvitz 1986; Shemer and Podbilewicz 2002). Previous investigations into the P3.p cell fate decision showed that its cell fate frequency is extremely sensitive to the dosage of

Wnt ligands, particularly *cwn-1*, suggesting that variability in the ligand concentration or in the response of the P3.p cell to Wnt ligands could provide the noise source driving the stochastic fate decision (Pénigault and Félix 2011a; b). In addition, mutations in the *C. elegans* Hox gene *lin-39* impact the Pn.p cell fate frequencies, by repression of cell fusion and promoting division of VPC fate cells (Clark *et al.* 1993; Maloof and Kenyon 1998; Koh *et al.* 2002; Shemer and Podbilewicz 2002; Roiz *et al.* 2016). Both Wnt signaling and LIN-39 inhibit hyp7/fusion fate, with loss-of-function mutants exhibiting increased frequency of cell fusion, including in the P4.p-P8.p cells that otherwise never assume hyp7/fusion fate (Gleason *et al.* 2006; Myers and Greenwald 2007). However, what aspects of Wnt signaling and LIN-39 dynamics control the frequency of hyp7/fusion versus VPC fate in P3.p remains unknown.

Here, we use a novel time-lapse microscopy approach (Gritti *et al.* 2016) to observe gene expression and signaling dynamics in single Pn.p cells during specification of the VPCs, allowing us to directly connect variability during the decision process to the final cell fate outcome. Using this approach, we found that BAR-1/ $\beta$ -catenin accumulated in a dynamic, pulsatile manner at the time of the hyp7/fusion versus VPC fate decision, with strong variability in pulse slope and timing. Combining quantitative data analysis with mathematical modeling, we found that cell fate outcome depended strongly on the time of the BAR-1/ $\beta$ -catenin pulse onset, identifying the timing of Wnt signaling dynamics as a key control parameter of cell fate.

# Results

## Time-lapse microscopy of a stochastic cell fate decision

So far, whether P3.p undergoes fusion or assumes VPC fate in wild-type or mutant animals has been assessed only after the process has completed (Eisenmann *et al.* 1998; Alper and Kenyon 2001, 2002; Chen and Han 2001; Myers and Greenwald 2007; Pénigault and Félix 2011b; a). To correlate early stochastic molecular events to eventual cell fate outcome it is essential to follow these processes directly in time. Here, we utilize a fluorescent time-lapse microscopy approach we developed recently to study single-cell dynamics inside moving and feeding *C. elegans* larvae for their entire ~40hr development (Gritti *et al.* 2016). We tested whether we could directly observe the occurrence of P3.p fusion events inside single animals. We initially used two measures of cell fusion: first, imaging the apical junction protein AJM-1, which localizes on the apical edge of Pn.p cells but is degraded upon cell fusion (Brabin *et al.* 2011). Second, observing the flow of GFP from the hypodermis into the fused Pn.p cell, using animals carrying an extrachromosomal array targeting GFP expression to the hyp7 hypodermal syncytium. Initially the AJM-1::mCherry signal expanded along the A-P axis during the early L2 larval stage (Supplementary Movies 1-2, Fig. 1c). In animals with a fusing cell, this was followed by a sudden and pronounced ruffling of the AJM-1::mCherry signal and a rapid retraction of AJM-1::mCherry towards the posterior, with the fluorescent signal fully disappearing from P3.p within 1 hr (Fig. 1c). Inflow of GFP from the hypodermis into P3.p was observed as soon as AJM-1::mCherry retraction commenced (Fig. 1c,d), showing that both are accurate markers of (the time of) fusion. Because AJM-1 was more easily monitored, we used AJM-1 dynamics to establish fate and timing of P3.p fusion for all subsequent experiments

Even though changes to the frequency of P3.p hyp7/fusion versus VPC fate in mutants are well studied (Eisenmann *et al.* 1998; Alper and Kenyon 2001, 2002; Chen and Han 2001; Myers and Greenwald 2007; Pénigault and Félix 2011b; a), it was not known how such mutants impact the timing of this decision. We quantified the time of P3.p fusion in wild-type animals and found that cell fusion occurred in a relatively narrow time window between 40-60% of the L2 larval stage (Fig. 1f). We then examined mutants in which fusion frequency is increased by removing inhibitory Wnt signaling or LIN-39 (Fig. 1b). We found that in these mutants P3.p fusion occurred within the same time window as wild-type animals, with only small differences between wild-type and mutant animals in average timing (Fig. 1f). Strikingly, even though the exact time of fusion can vary as much as 2 hrs between animals, when multiple VPCs fuse in a single animal, they typically do so at the same time (Fig. 1g). The observation that, in the absence of key repressors of hyp7/fusion fate, cell fusion frequency is increased independently of its timing provides evidence that a yet-unknown signal exists that activates cell fusion at the appropriate time. In contrast, hyp7/fusion inhibitors (Wnt signaling, LIN-39) do not control timing of fusion, but rather modulate hyp7/fusion versus VPC fate frequency.

## Stochastic *eff-1* induction precedes P3.p fusion

The most downstream regulator of the *hyp7*/fusion versus VPC fate decision is the gene *eff-1*, a fusogenic protein whose expression is sufficient to induce cell fusion (Mohler *et al.* 2002; Shemer *et al.* 2004). EFF-1 is a transmembrane protein that is required for most cell fusions in *C. elegans*, and must be present on both the Pn.p and *hyp7* plasma membrane to induce fusion (Zeev-Ben-Mordehai *et al.* 2014; Smurova and Podbilewicz 2016). To understand how cell fate frequency is regulated on the level of *eff-1* expression, we counted *eff-1* mRNA molecules in Pn.p cells, using single molecule FISH (smFISH) (Raj *et al.* 2008). In wild-type animals where P3.p had not undergone fusion, based on presence of the AJM-1 signal, we most frequently observed low *eff-1* expression in P3.p, <5 molecules (Fig. 2a,c,d), similar to the P4.p cell that always assumes VPC fate in wild-type animals (Fig. 2c,d). However, in the range of body lengths (340-380  $\mu$ m) corresponding to the measured time of fusion, we observed a subset of wild-type animals expressing much higher *eff-1* levels, ~30-50 molecules (Fig. 2b-d). We found that high *eff-1* expression was maintained in fused P3.p cells, before disappearing by the end of the L2 stage (Supplemental Fig. 1a,b). We confirmed that high *eff-1* expression preceded cell fusion, rather than following it, by examining a temperature-sensitive loss-of-function point mutation in *eff-1* (Mohler *et al.* 2002). Here, we still found high *eff-1* mRNA levels in P3.p at the restrictive temperature, even as P3.p cell fusion was fully inhibited (Supplemental Fig. 1c).

When we examined the distribution of *eff-1* mRNA levels in P3.p, we found a broad peak of P3.p cells with low *eff-1* mRNA levels (<20 molecules) that was similar to that seen in the non-fusing P4.p cell and a much smaller peak at ~40 *eff-1* mRNAs that was not observed in P4.p, indicating that such high levels correspond to P3.p cells about to assume *hyp7*/fusion fate. An interesting result is that the fraction of wild-type animals showing high (>20 molecules) *eff-1* mRNA levels in P3.p was significantly smaller than the expected fraction of animals where P3.p assumes *hyp7*/fusion fate (Fig. 2d). For our analysis, we randomly sampled animals within the time window we expected fusion to occur. Given the observed variability in the time of fusion (Fig. 1f), it is expected that some animals with low *eff-1* expression would have ultimately fused at a later point. In particular, the fraction of animals observed with high *eff-1* expression in unfused P3.p cells should increase with the average duration the cell expresses high *eff-1* before this results in fusion. Hence, our results suggested that induction of high *eff-1* expression was quickly followed by cell fusion.

To understand how *eff-1* expression impacts cell fate frequency, we quantified *eff-1* levels in a strain with a functional LIN-39::GFP insertion (*lin-39(++)*) that caused low fusion frequency (~2% P3.p fusion frequency). The resulting *eff-1* distribution was similar to wild-type for low *eff-1* levels, but lacked the highly expressing P3.p cells (Fig. 2e). In contrast, in the *cwn-1(0)* mutant that lacks the dominant Wnt ligand and exhibited high (>80%) fusion frequency both in P3.p and P4.p, we found that the fraction of cells in the high *eff-1* peak had increased substantially, in particular in P4.p, even though the position of this peak itself had not shifted (Fig. 2f). Together, this indicated that Wnt signaling and LIN-39 controlled cell fate frequency mainly by tuning the fraction of cells in which high *eff-1* expression is induced.

## No bias of cell fate decision by noise in LIN-39 protein level

The Hox transcription factor LIN-39 inhibits Pn.p hyp7/fusion fate by repressing *eff-1* expression (Shemer and Podbilewicz 2002), with *lin-39* null mutations causing all Pn.p cells to fuse in the L1 larval stage (Clark *et al.* 1993; Wang *et al.* 1993). Hence, stochastic variability in LIN-39 protein levels could result in variability in induction of high *eff-1* expression. It was shown previously that LIN-39 levels are similar between P3.p and P4.p in early L2 larval stage animals prior to cell fusion (Pénigault and Félix 2011a), even though both cells have a different fate frequency (Fig. 1b). However, individual cells were not followed over time and it is possible that small differences in LIN-39 between P3.p cells in different animals are sufficient to explain the outcome. To connect animal-to-animal variability in LIN-39 level with P3.p cell fate, we performed time-lapse microscopy on animals carrying a *lin-39::GFP* translational fusion (Sarov *et al.* 2012) and *ajm-1::GFP* as a cell fusion marker (Fig. 3a,b). Since *lin-39::GFP* (*lin-39*(++)) is present as a multi-copy insertion, it decreased the P3.p fusion rate from ~30% to ~2%, making it challenging to capture sufficient P3.p fusion events for analysis. For that reason, we further crossed these reporters into the *cwn-1(0)* mutant, increasing the P3.p and P4.p fusion rates to 20% and 14%, respectively.

We observed that LIN-39 was present in the P3.p nucleus at the start of the L2 larval stage and remained there for the entire larval stage when P3.p assumed VPC fate (Fig. 3a,c). However, in P3.p cells that fused, nuclear LIN-39 levels decreased rapidly after fusion commenced and fully disappeared within 90 mins (Fig.3b,c), consistent with past observations of loss of LIN-39 in fused Pn.p cells (Pénigault and Félix 2011a). We compared the distribution of LIN-39 levels, averaged over 3 hrs prior to fusion in P3.p cells that assumed hyp7/fusion fate with the distribution in P3.p cells that assumed VPC fate, averaged over 3hrs prior to the average time of P3.p fusion in this strain (Fig. 3d). We found strong overlap between the two distributions, also when changing the size of the time window (data not shown), making it unlikely that fluctuations LIN-39 levels drive stochastic *eff-1* induction and cell fusion.

## $\beta$ -catenin activation dynamics during the cell fate decision

We next quantified activation of the Wnt pathway by monitoring the accumulation dynamics of BAR-1/ $\beta$ -catenin in a strain carrying a functional *bar-1::GFP* reporter (*bar-1*(++)) (Eisenmann *et al.* 1998). In the absence of Wnt ligands,  $\beta$ -catenin is continuously degraded by a degradation complex. Upon activation of Wnt receptors by Wnt ligands, activity of the degradation complex is stopped, allowing  $\beta$ -catenin to accumulate in the cell and nucleus (Sawa and Korswagen 2013). In P3.p, the presence of BAR-1 is required to inhibit *eff-1* expression and, hence, inhibit hyp7/fusion fate (Eisenmann *et al.* 1998). In contrast to  $\beta$ -catenins involved in the Wnt asymmetry pathway (Park and Priess 2003; Mila *et al.* 2015), dynamics of BAR-1 during canonical Wnt signaling is poorly characterized. Because Wnt ligands are expressed continuously during larval development (Coudreuse *et al.* 2006), we expected BAR-1 to show constant expression and dynamics in P(3-8).p cells, similar to LIN-39. Instead, we found that BAR-1::GFP levels were strikingly dynamic, with no BAR-1::GFP in P(3-8).p at the start of the

L2 stage, followed by pulse of BAR-1::GFP in P(3-8).p at the mid-L2 stage that lasted 1-4 hours and was strongly coordinated between cells (Supplemental Movie 3, Fig. 4a-c). BAR-1 was detected both in the nucleus and cytoplasm. We found stochastic variability in the amplitude of the BAR-1 pulse between different Pn.p cells (Fig. 4b,c). It was speculated that P3.p, which is considered most distant to the source of Wnt ligands, receives a lower Wnt signal than P(4-8).p, thereby resulting in its occasional hyp7/fusion fate (Harterink *et al.* 2011; Pénigault and Félix 2011b). However, the BAR-1::GFP pulse in P3.p was frequently of similar or higher amplitude compared to the other Pn.p cells and, in general, we found no sign of a systematic spatial pattern in Wnt signaling. We also found significant variability in the amplitude and timing of the BAR-1::GFP pulse in the P3.p cell compared between different animals (Fig. 4d).

Since the BAR-1::GFP reporter is integrated as a functional multi-copy transgene, we expected this strain to act as a BAR-1 overexpression mutant and, indeed, observed no P(3-8).p cell fusions (Supplemental Table 1). Hence, we refer to this strain as *bar-1(++)*. To study how BAR-1 dynamics related to cell fate frequency, we used different approaches to increase the frequency of hyp7/fusion fate. First, we decreased the level of the inhibitor LIN-39, using the *lin-39(n709)* temperature sensitive loss-of-function mutant, leading to 16/70 P3.p cells assuming hyp7/fusion fate in *bar-1(++);lin-39(lf)* animals (Supplemental Table 1). We found that *bar-1(++);lin-39(lf)* animals showed similar BAR-1::GFP pulses (Fig. 4e). Cells that fused always did so during the early accumulation phase of the BAR-1 pulse (Fig. 5a). Next, we sought to lower BAR-1 levels in the *bar-1(++)* background by decreasing activity of the Wnt signaling pathway, using the *cwn-1(0)* mutant that lacks the CWN-1 Wnt ligand (Fig. 1a). In these animals, BAR-1::GFP pulse amplitude was lower (Fig. 4f). In some *bar-1(++);cwn-1(0)* animals the L2 stage was significantly lengthened. Moreover, we found that BAR-1::GFP pulses occurred at significantly later times, as fraction of larval stage duration, even in animals with similar duration as the other mutants. Finally, BAR-1 pulses also showed considerable variability in timing and amplitude in these mutants.

## Variability in $\beta$ -catenin pulse dynamics

To characterize variability in BAR-1 accumulation dynamics, we used a minimal parameterization of the BAR-1 pulse to fit to the experimental data (Fig. 5a, Eq. 3 in Methods). Briefly, we assume that prior to the BAR-1 pulse, Wnt signaling is inactivated and BAR-1 is degraded. At pulse onset time  $t_0$ , Wnt signaling is activated, leading to inhibition of BAR-1 degradation and hence linear accumulation of BAR-1 in the cell. Linear BAR-1 accumulation continues for a pulse duration  $T$  in cells that assume VPC fate or until the time of fusion,  $t_{\text{fusion}}$ , in cells that assume hyp7/fusion fate. Upon fusion BAR-1 vanishes immediately, as observed experimentally, whereas in cells that assume VPC fate, BAR-1 levels decrease exponentially once the pulse ends. This fitted the experimental data surprisingly well (Fig. 5a,b). Moreover, it allowed us to describe each BAR-1 pulse by three parameters: pulse onset time  $t_0$ , pulse slope  $s$  and pulse duration  $T$  for VPC cells or fusion time  $t_{\text{fusion}}$  for hyp7/fusion cells.

First, we compared the distribution of pulse onset time  $t_0$  and linear slope  $s$  of BAR-1 accumulation pulses between strains. We found that both were highly variable between animals

in all strains (Fig. 5c,d). We found that the pulse parameters of *bar-1(++)* and *bar-1(++);lin-39(lf)* were similar, consistent with increase in hyp7/fusion fate frequency in this mutant resulting from the absence of the fusion inhibitor LIN-39 rather than changes in Wnt signaling. In contrast, we assumed that the increase in frequency of hyp7/fusion fate in *bar-1(++);cwn-1(0)* animals was due to a decrease in BAR-1 level. In the context of the observed BAR-1 pulses this could be achieved in two independent ways, either by decreasing the slope  $s$  or by delaying the onset time  $t_0$  of the BAR-1 pulse relative to the time of fusion (Fig. 6a,b). Given that BAR-1 accumulation is thought to be proportional to the amount of external Wnt ligands, we expected the *cwn-1(0)* mutant, that lacks the CWN-1 Wnt ligand, to have a decreased rate of BAR-1 accumulation. Surprisingly, we found that the pulse slope distribution was highly similar for *bar-1(++)* and *bar-1(++);cwn-1(0)* animals (Fig. 5c) and that the only different pulse characteristic was the delayed pulse onset (Fig. 5d).

We then compared the timing of the onset of BAR-1 accumulation between P3.p and P4.p cells. Both in *bar-1(++)* and *bar-1(++);lin-39(lf)* animals, considerable variability existed in  $t_0$ , the time of the onset of the BAR-1 pulse, between these cells, with BAR-1 accumulation in P3.p preceding that in P4.p as often as the reverse (Fig. 5b,e). At the same time, pulse onset was correlated between P3.p and P4.p, meaning that if BAR-1 accumulation started late in the L2 larval stage in P3.p, it was also likely to start late in P4.p (Fig. 5e). Strikingly, we not only found that in the *bar-1(++);cwn-1(0)* mutant the onset of the BAR-1 pulse was delayed, but also that the variability in pulse onset time between P3.p and P4.p was almost completely removed, with the onset of BAR-1 accumulation occurring in P3.p and P4.p within 20 min in all animals (Fig. 5e). This result suggests that the Wnt ligand *cwn-1* not only controls the average onset of BAR-1 pulses, but also induces variability in pulse onset time between P3.p and P4.p.

We also observed variability in the duration of BAR-1 pulses when comparing pulses in the same cell between animals (Fig. 5b,f). We examined whether the onset and the duration of BAR-1 pulses were correlated. Because the duration of the L2 larval stage varied significantly between strains and animals, we examined the pulse onset time  $t_0/T_{L2}$  and duration  $T/T_{L2}$  relative to the duration of the larval stage,  $T_{L2}$ . In this case, we found a striking anti-correlation, with late pulse onset resulting in shorter pulses (Fig. 5f). In fact, the data for all strains clustered along the line  $T/T_{L2} = 0.66 - t_0/T_{L2}$ , consistent with a model in which the end of the BAR-1 accumulation occurs at 66% of the L2 larval stage independent of the BAR-1 pulse onset time. This correlation also held for the *bar-1(++);cwn-1(0)* mutant, where not only the onset of BAR-1 pulses was delayed but also the L2 larval stage was much extended. Hence, the BAR-1 pulse ended independent of its onset time  $t_0$  in all mutants examined.

Given that we observed strong variability in pulse onset time relative to the time the pulse ceases (Fig. 5f), we asked whether the time of cell fusion was correlated with either the pulse start or end time. However, because cell fusion is immediately followed by rapid degradation of BAR-1, it was not possible to determine the pulse end time in cells that assumed hyp7/fusion fate. At the same time, P4.p cells often assumed hyp7/fusion fate in *bar-1(++);lin-39(lf)* and *bar-1(++);cwn-1(0)* animals. Therefore, we selected animals where one Pn.p cell, either P3.p or P4.p, assumed hyp7/fusion fate whereas the other assumed VPC fate. We then



compared within the same animal the fusion time  $t_{\text{fusion}}$  in the hyp7/fusion cell with the pulse onset time  $t_0$  (Fig. 5g) or the pulse end time  $t_0 + T$  (Supplemental Fig. 2) in the VPC. For *bar-1(++);lin-39(lf)* animals, the time of fusion correlated most strongly with the pulse onset time ( $R=0.86$ , P3.p fusing only) rather than pulse end time ( $R=0.56$ ). Specifically, the data clustered along the line  $t_{\text{fusion}}/T_{L2} = 0.2 + t_0/T_{L2}$ , i.e. cell fusion occurs at a time  $0.2T_{L2}$ , or on average  $\sim 2$  hrs, after the onset of the BAR-1 pulse. Because the *bar-1(++);cwn-1(0)* mutant has the same pulse slope distribution as the *bar-1(++)* mutant (Fig. 5c), we examined whether the increased hyp7/fusion frequency in the *bar-1(++);cwn-1(0)* mutant was due to a shorter delay between pulse onset and time of fusion. Indeed, we found that in *bar-1(++);cwn-1(0)* animals the delay was halved, with cell fusion now occurring at a time  $0.1T_{L2}$  after onset of the BAR-1 pulse (Fig. 5g). We found before that *bar-1(++);cwn-1(0)* animals have a similar rate of BAR-1 accumulation as *bar-1(++)* (Fig. 5c). Delaying the pulse onset relative to the time of fusion would be an alternative mechanism to lower inhibitory BAR-1 levels.

## Bias of cell fate decision by variability in $\beta$ -catenin pulse timing

To elucidate the mechanism by which BAR-1 pulse dynamics might impact *eff-1* expression and cell fate frequency, we constructed a mathematical model of the cell fate induction network that takes into account variability in BAR-1 pulse slope and timing (Fig. 6a-c, see Materials and Methods for details). In the model, hyp7/fusion fate requires sufficiently high *eff-1* expression. We assumed that an activator controls the timing of cell fusion in the absence of the fusion inhibitors BAR-1 and LIN-39, consistent with our observations in Fig. 1f. In contrast, BAR-1 and LIN-39 then modulate cell fate outcome by inhibiting *eff-1* expression. Specifically, *eff-1* expression is induced only when the activator, but not BAR-1 and LIN-39 are bound to the *eff-1* promoter (Fig. 6a). Here, BAR-1 is expected to control *eff-1* expression in a complex with the Wnt effector POP-1 (Korswagen *et al.* 2000). In the model, we assumed that the activator is only present from time  $t_{\text{fusion}}$  at a level  $c_a$  (Fig. 6b). Also, we assumed that the level of the inhibitor Wnt signal,  $c_W(t)$ , followed the observed BAR-1 dynamics, rising from the pulse onset time  $t_0$  with linear slope  $s$  (Fig. 6b). Finally, we assumed stochastic variability in activator level, pulse slope and time of pulse onset and fusion.

We constrained almost all model parameters by experimental data (See Materials and Methods) as follows: using experimentally measured correlations between i) pulse onset time in different cells and ii) pulse onset time and time of fusion in the same cell, we estimated the relative contributions of global and cell-specific variability in timing of pulse onset and cell fusion. Next, we fitted the observed distribution of pulse slopes by a Gaussian distribution (Supplemental Fig. 3a). Finally, we adjusted the parameters governing the action of LIN-39 and the activator to reproduce the observed hyp7/fusion frequency in the different strains (Supplemental Fig. 3e). For all mutants, the resulting model provided an excellent fit to the observed distributions of pulse onset time  $t_0$  and slope  $s$  (Supplemental Fig. 3a-d), the joint distribution of  $t_0$  in P(3,4).p (Supplemental Fig. 3f) and that of  $t_0$  and fusion time  $t_{\text{fusion}}$  (Supplemental Fig. 3g). In the model, the increased frequency of hyp7/fusion fate in *bar-1(++);lin-39(lf)* animals was due to absence of LIN-39 increasing the range of activating and inhibitory

signals  $c_a$  and  $c_w$  for which *eff-1* is expressed sufficiently highly, whereas in the *bar-1(++);cwn-1(0)* mutant, the reduced delay between  $t_0$  and the time,  $t_{\text{fusion}}$ , when the activator becomes available causes lower inhibitory Wnt signals  $c_w$  at  $t_{\text{fusion}}$  (Supplemental Fig. 3e). We used the model to examine a hypothetical mutant that achieves the same hyp7/fusion frequency as the *bar-1(++);cwn-1(0)* mutant, but by changing pulse slope rather than pulse onset time. We found that this mutant was clearly distinguishable from the *bar-1(++);cwn-1(0)* mutant in terms of pulse slope distribution and delay between pulse onset and time of fusion (Supplemental Fig. 3b,g), providing further evidence that the change in pulse timing is the key reason hyp7/fusion fate is increased in the *bar-1(++);cwn-1(0)* mutant.

We next used the model to ask whether variability in BAR-1 pulse timing impacts the outcome of individual cell fate decisions, focusing on the *bar-1(++);lin-39(lf)* mutant that produced most hyp7/fusion cells. We examined the difference in pulse slope and onset time in *bar-1(++);lin-39(lf)* animals, comparing animals where P3.p fused but P4.p assumed VPC fate with animals where both P3.p and P4.p assumed VPC fate. The model predicted that for animals where both cells assume VPC fate, the distributions  $P(s_{P4.p}-s_{P3.p})$ , of difference in pulse slope, and  $P(t_{0,P4.p}-t_{0,P3.p})$ , of difference in pulse onset time, are symmetrical (Fig. 6d,f, blue line). However, the model predicted a bias towards low pulse slope and late pulse onset time in fusing P3.p cells compared to non-fusing P4.p cells (Fig. 6d,f, red line), because both decrease the amount of inhibitory BAR-1. In agreement with the model, we found that the experimentally obtained distributions of difference in pulse slope and onset time between P3.p and P4.p were symmetrical, both in *bar-1(++)* animals, where P(3,4).p never fuse, and *bar-1(++);lin-39(lf)* animals selected so that both cells assumed VPC fate (Fig. 6e,g, black and blue lines). However, in *bar-1(++);lin-39(lf)* animals where P3.p, but not P4.p, assume hyp7/fusion fate, we found a weak bias towards lower pulse slope in P3.p and a significantly stronger bias towards delayed BAR-1 pulse onset in fusing P3.p cells compared to non-fusing P4.p cells (Fig. 6e,g, red line), with only one animal with a fusing P3.p cell showing BAR-1 accumulation in P3.p prior to P4.p. This difference was particularly striking compared to the *bar-1(++)* strain, which otherwise showed no difference in relative timing of BAR-1 pulse onset between P3.p and P4.p relative to *bar-1(++);lin-39(lf)* animals (Fig. 5c).

Even though the above results indicated that BAR-1 pulse timing biased the hyp7/fusion versus VPC fate decision, it left open whether variations in pulse timing achieve this by specifically modulating BAR-1 levels at the time the decision to fuse or not is made. The model predicted that at the time of fusion cells assuming hyp7/fusion fate in *bar-1(++);cwn-1(0)* mutants should have lower BAR-1 levels than fusing cells in *bar-1(++);lin-39(lf)* mutants, where fusion frequency is instead increased by removing the inhibitor LIN-39 (Fig. 6h). Indeed, when we compared BAR-1::GFP fluorescence at the time of cell fusion in *bar-1(++);lin-39(lf)* and *bar-1(++);cwn-1(0)* animals, we found a bias towards lower BAR-1 levels in fusing P3.p and P4.p cells in the *cwn-1(0)* background (Fig. 6i). To further link BAR-1 levels to inhibition of cell fusion, we quantified *eff-1* transcripts in *bar-1::gfp* animals and indeed found a negative correlation: Pn.p cells with visible BAR-1::GFP had few *eff-1* transcripts, while unfused Pn.p cells without BAR-1::GFP often showed high *eff-1* levels (Supplemental Figure 4). Together, these results show that changes in the timing of BAR-1 accumulation pulses are a key determinant of the

hyp7/fusion versus VPC fate decision, likely by impacting the BAR-1 level at the time of the decision.

# Discussion

## Pulsatile BAR-1/ $\beta$ -catenin dynamics

Here, we combined a novel time-lapse microscopy approach with quantitative analysis and mathematical modeling to study, in developing *C. elegans* larvae, how the outcome of a stochastic cell fate decision is controlled by random variability in the dynamics of the underlying signaling network. Surprisingly, we found that BAR-1/ $\beta$ -catenin, a core component of the Wnt pathway, accumulated in Pn.p cells in a dynamic, pulsatile manner (Fig. 4) that was precisely timed to influence their stochastic choice between vulva precursor or hypodermal fate, with the latter fate inhibited by BAR-1/ $\beta$ -catenin. Moreover, we found that the timing of the BAR-1/ $\beta$ -catenin pulse was a key control parameter influencing the relative frequency of these two cell fates: first, we observed that the increase in hypodermal fate frequency in *bar-1(++);cwn-1(0)* mutants, compared to that in *bar-1(++)* mutants, was not due to systematic changes in the slope of the BAR-1/ $\beta$ -catenin pulse, but rather to a systematic decrease in the time delay between the pulse onset and the time of the cell fusion event that defines hypodermal fate (Fig. 5). Second, in the *bar-1(++);lin-39* mutant we found that Pn.p cells that assume hypodermal fate have a later pulse onset than those cells in the same animal that assume vulva precursor fate (Fig. 6). Experiments and modeling suggest that pulse timing influences the cell fate decision by changing the level of BAR-1/ $\beta$ -catenin, and hence the amount of inhibition of hypodermal fate, at the time that hypodermal fate and cell fusion are induced (Fig. 6). Overall, these results indicate that for the cell fate decision studied here, it is not the absolute BAR-1/ $\beta$ -catenin level per se, as is generally assumed, but rather the timing of its accumulation dynamics relative to other developmental events, that is a key factor determining cell fate outcome.

## Mechanism of BAR-1/ $\beta$ -catenin pulse generation

A striking feature of BAR-1/ $\beta$ -catenin pulse dynamics is their complex timing: despite considerable differences in time of pulse onset, both between mutants (Fig. 5d) and between Pn.p cells within the same mutant (Fig. 5e), pulse dynamics is otherwise synchronized between the multiple adjacent Pn.p cells (Fig. 4), with the time of the end of the pulse highly similar in all mutants (Fig. 5f). It is an important question how the BAR-1/ $\beta$ -catenin pulse is generated. BAR-1/ $\beta$ -catenin accumulation could be controlled by changes in the level of the Wnt ligands outside of the cell or rather by changes in the Wnt pathway components inside the cell, such as changes to Wnt receptor levels or presence/activity of components of the  $\beta$ -catenin destruction complex. We currently favor the latter hypothesis, since neuronal cells close to the Pn.p cells show BAR-1::GFP expression in the late L1/early L2 stage when Pn.p cells do not, with a significantly decreased BAR-1::GFP signal in those cells in a *cwn-1(0)* background. This suggests that Wnt ligands are already present and able to activate Wnt signaling at this time and position in the body.

Our observations differ significantly from the current model of Wnt signal propagation at a number of points. First, as ligand-activated Wnt receptors sequester and thereby inactivate

the destruction complex that induces  $\beta$ -catenin degradation, it was expected that changing Wnt levels would predominantly impact the rate of  $\beta$ -catenin accumulation (Clevers and Nusse 2012; Sawa and Korswagen 2013). However, using the *cwn-1(0)* mutant we found that removing a Wnt ligand instead changed only the timing of the induced BAR-1/ $\beta$ -catenin pulse (Fig. 4, 5c,d), which is difficult to explain based on our current knowledge of the Wnt pathway. Particularly surprising is that loss of *cwn-1* almost completely removed the variability in BAR-1/ $\beta$ -catenin pulse timing between adjacent Pn.p cells in the same animal (Fig. 5e). In absence of CWN-1, other Wnt ligands such as EGL-20 repress hypodermal fate, albeit at reduced efficiency (Pénigault and Félix 2011b). Our results indicate that CWN-1 acts in a significantly more stochastic manner, either on the level of ligand/receptor interaction or the delivery of ligands to the Pn.p cells, than the other Wnt ligands in the body, even though it is the Wnt ligand expressed closest to the Pn.p cells (Eisenmann 2005; Harterink *et al.* 2011). It was also suggested that cells respond to fold change rather than the absolute level of  $\beta$ -catenin (Goentoro and Kirschner 2009). However, this is inconsistent with our observation that cell fate frequency is impacted by changes in timing of BAR-1/ $\beta$ -catenin pulse onset, which do not impact fold change, rather than changes in pulse slope (Fig. 5c,d). Moreover, we find higher levels of inhibitory BAR-1/ $\beta$ -catenin at the time of cell fusion in mutants that lack the parallel hypodermal/fusion fate inhibitor LIN-39 (Fig. 6i), another indication that absolute BAR-1/ $\beta$ -catenin levels control the frequency of hypodermal fate.

It is an open question how the decay of the BAR-1/ $\beta$ -catenin pulse is controlled. Negative feedback of the Wnt/ $\beta$ -catenin pathway has been shown to occur through the regulator Axin, which could be responsible for shutting off  $\beta$ -catenin accumulation (Jho *et al.* 2002). However, this negative feedback model implies that the end of the pulse would be tightly linked to the pulse onset, rather than occurring at a fixed point in the larval stage independent of the start of the pulse, as we observed (Fig 5f). We speculate, based on the link between the BAR-1/ $\beta$ -catenin pulse end time and the timing of the larval stage, that this aspect of pulse timing is regulated by the molting cycle. In particular, it has been shown that many genes show body-wide gene expression oscillations, peaking once every larval stage but at different phases (Hendriks *et al.* 2014). Some of these genes might be responsible for switching of BAR-1/ $\beta$ -catenin accumulation in all Pn.p cells simultaneously. Our data indeed suggested that a Wnt-independent timing mechanism is present, as the time of cell fusion was unperturbed in a *bar-1(0)* mutant (Fig. 1f). In general, our observations suggest that timing of BAR-1/ $\beta$ -catenin accumulation dynamic can be regulated both by Wnt-dependent signals and Wnt-independent developmental timing cues.

## Role of $\beta$ -catenin pulses in development

It is increasingly clear that many of the canonical metazoan signaling pathways control development using temporal information encoded in their dynamics (Shimojo *et al.* 2008; Levine *et al.* 2013) In particular, pulses in the output of signaling pathways have now been identified *in vivo* in a number of developmental systems. For example, a recent study showed that EGF signaling acts in a pulsatile manner in the VPCs, with signaling strength transmitted in the frequency of pulses instead of a continuous graded signal (de la Cova *et al.* 2017). Moreover,

time-lapse imaging of oscillatory, rather than pulsatile dynamics of Notch and Wnt signaling during segmentation of mouse embryos showed that the relative phase of the two oscillations instructs the segmentation process by an unknown mechanism (Sonnen *et al.* 2018). In this study Wnt signaling was monitored indirectly, using an Axin rather than a  $\beta$ -catenin reporter. So far, the dynamics of  $\beta$ -catenin accumulation have rarely been studied directly. Pulses of  $\beta$ -catenin have been observed (Murphy *et al.*, 2014, Kafri *et al.*, 2016), although mostly in cell lines following exogenous application of Wnt ligands rather than in the natural context of the body. For all these studies, differences in timing of  $\beta$ -catenin pulses have not been linked to cell fate outcome.

It remains an open question what the advantage is of pulsatile BAR-1/ $\beta$ -catenin dynamics for the hypodermal versus VPC decision, as opposed to the constant expression level displayed by the parallel hypodermal fate inhibitor LIN-39 (Fig. 3). So far, our limited observations have not revealed BAR-1 pulsatile dynamics for other canonical Wnt signaling processes during larval development. Our mathematical model indicates one potential advantage, namely that BAR-1/ $\beta$ -catenin pulsatile dynamics allows for pulse timing as an additional control parameter, next to BAR-1/ $\beta$ -catenin accumulation rate, to tune cell fate frequency (Fig. 6). Which cells receive Wnt input is tightly controlled in space, e.g. by regulating Wnt receptor expression. In contrast, pulsatile dynamics of signaling pathways could be a powerful mechanism to control precisely when cells respond to ligands in time. This might be particularly important because the same signaling pathways are used many times during development, sometimes even in the same cell, to control different developmental events. Reading out these signaling pathways only at particular time points, using pulsatile dynamics, would allow the reconfiguration of the pathway from executing one developmental decision to another. Interestingly, Wnt signaling is used in VPCs at the mid-L3 stage,  $\sim$ 10 hrs after the hypodermal versus VPC decision, to control the anteroposterior orientation of the asymmetric divisions of the VPCs (Green *et al.* 2008). Here, EGL-20 plays an important role, whereas BAR-1 and CWN-1 have a smaller contribution. The decay of the BAR-1/ $\beta$ -catenin pulse at the end of the L2 stage might be crucial to avoid temporal crosstalk between the outputs of the Wnt pathway as the VPCs transition from one process to the next.

In conclusion, we have shown here that  $\beta$ -catenin accumulation can be highly dynamic during development, with temporal information instructing development contained in its dynamics. Many (stochastic) cell fate decisions in organism from nematodes to humans are controlled by Wnt signaling and it will be interesting to see whether pulsatile  $\beta$ -catenin plays a similar role in biases cell fate frequencies in those systems. The quantitative approach we employed here, combining *in vivo* time-lapse imaging of  $\beta$ -catenin dynamics with measurements of key dynamical parameters such as pulse slope and pulse timing, can provide a template for such future studies.

# Materials and Methods

## CONTACT FOR REAGENT AND RESOURCE SHARING

Further information and requests for resources and reagents should be directed to and will be fulfilled by the Lead Contact, Jeroen van Zon (j.v.zon@amolf.nl).

## EXPERIMENTAL MODEL DETAILS

### Strains

All strains were handled according to the standard protocol on Nematode growth medium (NGM) agar plates with OP50 bacteria (Brenner 1974). Experiments were performed on L2 stage hermaphrodites. Strains were obtained from the CGC unless otherwise indicated.

The following mutations were used in this study:

LGII: *cwn-1(ok546)* (The C. elegans Deletion Mutant Consortium 2012),

LGIII: *lin-39(gk893)* (The C. elegans Deletion Mutant Consortium 2012), *lin-39(n709)* (Clark *et al.* 1993)

LGX: *bar-1(ga80)* (Eisenmann *et al.* 1998)

The following transgenes were used in this study:

*ncls13[ajm-1::GFP]*, (Liu *et al.* 2005)

*sIs11337[rCesY37A1B.5::GFP + pCeh361]*,

*ouls20 [ajm-1::mCherry + unc-119+]* (gift from Alison Woollard),

*itIs37[pie-1p::mCherry::H2B::pie-1 3'UTR + unc-119(+)] IV*,

*stIs10116[his-72(promoter)::his-24::mCherry::let-858 3'UTR + unc-119(+)]*,

*stIs10311[lin-39::TGF(3D3)::GFP::TY1::3xFLAG]* (Sarov *et al.* 2012),

*gals45[pDE218(bar-1::bar-1::GFP)]* (gift from David Eisenmann) (Eisenmann *et al.* 1998), and

*stIs10226[his-72p::HIS-24::mCherry::let-858 3' UTR + unc-119+]*, (Sarov *et al.* 2012)].

The presence of the *cwn-1(ok546)* homozygous deletion was confirmed by nested PCR screening. The following primers were used: outer left ('5-TCGTTTCTGACATGGCTCAC-3'), outer right ('5-ACCCATCCTTTCCCAATCTC-3'), inner left ('5-CGTATCCACGACCACAACAG-3') and inner right ('5'-AGAATCTTACACCAACGGG-3').

## METHOD DETAILS

### Time-lapse imaging

The microchamber size used in the study was 190  $\mu\text{m}$  x 190  $\mu\text{m}$ , with a depth of 10  $\mu\text{m}$  and made as previously described and imaged with a custom time-lapse microscope (Gritti *et al.* 2016). Using an eyelash attached to a glass pipette, OP50 bacteria was used as "glue" to transfer eggs into the microchambers using M9 solution to keep the microchamber moist. A Nikon Ti-E inverted microscope with a large chip camera (Hamamatsu sCMOS Orca v2) and a 60 X magnification objective (NA=1.4 oil immersion) was used for imaging. Transmission imaging was performed using an LED light source (CoolLED pE-100 615nm), while 488 and 561 nm fluorescence images were acquired using Coherent OBIS LS 488-100 and OBIS LS 561-100 lasers, respectively. Images were acquired in a temperature controlled room at 19° with a

sample temperature of 22°. Exposure time was 10 ms and approximately 25 images were taken with a z-distance of 1 µm. Images were taken every 20 min. Images were 2048 x 2048 pixels and saved in 16-bit TIFF format. Fusion times were determined by *ajm-1::GFP* localization and morphology.

### Quantitative Image Analysis

For all experiments, transmitted light images were used to identify molt times. Custom Python scripts and ImageJ were used to quantitatively analyze the acquired images (Schindelin *et al.* 2012; Schneider *et al.* 2012). First, images to be used for quantitative analysis were corrected for uneven laser illumination in the following manner: flat field intensity for the particular experiment was obtained by imaging a uniformly fluorescent (488nm) testing slide, and averaging the result of 10 images. We divided each pixel's intensity value in the experimental images by the corresponding flat field pixel's intensity, normalized to the median value of the entire flat field image. This normalization procedure corrects for position-dependent variation in light intensity due to the Gaussian profile of the laser beam. The region of interest was cropped at this time. Pn.p cells were manually identified by stereotyped nuclear position location and the domains of *ajm-1::gfp/mcherry* expression, if present. To measure *lin-39::gfp* expression, a mask was manually drawn around the nucleus and the mean fluorescence intensity of the pixels within the mask was calculated. The z-slice closest to the center of the nucleus was used. A background fluorescence measurement for each image was obtained by creating a mask of the intranuclear space in a region near P3.p and P4.p along the axis of the ventral nerve cord. The mean background fluorescence value was then subtracted from the mean fluorescence value of the reporter for the same image. To measure *bar-1::gfp* expression, a mask was manually drawn around the Pn.p cytoplasmic region using *ajm-1::mCherry* signal as a positional guide, with background corrections performed similarly as described above. For the Supplementary Movies, fluorescence images were computationally straightened and aligned, using the animal's body shape and position of the Pn.p cells as measured from the fluorescent markers.

### Single-molecule fluorescence in situ hybridization (smFISH)

Probe design and smFISH hybridization to visualize *eff-1* mRNA transcripts were performed as previously described (Raj *et al.* 2008; Huelsz-Prince and van Zon 2017). Custom probes were designed against the exons of the *eff-1* gene by utilizing the Stellaris® RNA FISH Probe Designer (Biosearch Technologies, Inc., Petaluma, CA). The probes were hybridized with the Cy5 dye (Huelsz-Prince and van Zon 2017). The sequences of the oligonucleotide probes used in this study are listed in Table 1 of the Supplementary Methods. Animals were collected by washing plates with M9 and were fixed in 4% formaldehyde in 1 X PBS for 45 min at room temperature. Fixed animals were permeabilized in 70% ethanol at least one night at 4°C. Subsequently, animals were incubated with the 0.5 µl probes overnight at 30°C in Stellaris® Hybridization Solution containing 10% formamide. The next day, animals were quickly washed two times with 10% formamide and 2 X SSC, followed by an incubation wash for 30 min at 30°C. DAPI was added at 0.01 µg/ml in a final incubation step for 20 min at 30°C. Animals were mounted in Glox Buffer with catalase and glucose oxidase, and images were acquired with a Nikon Ti-E inverted fluorescence microscope, equipped with a 100X plan-apochromat oil-



immersion objective and an Andor Ikon-M CCD camera controlled by  $\mu$ Manager software (Edelstein *et al.* 2014). Stacks of each animal were taken with a z-distance of 0.33  $\mu$ m and approximately 30 images were taken per animal. Cy5 exposure time was 3 s, while DAPI and GFP exposure time were 100 ms and 500 ms, respectively. Animals were then imaged at 40X to determine their body length, which was measured using ImageJ by drawing a spline from the tip of the head to the end of the tail. smFISH images were analyzed with a custom Python script using techniques previously described (Raj *et al.* 2008). The *ajm-1::gfp* transgene was used to determine the cell fusion status. To construct *eff-1* distributions in P3.p and P4.p cells prior to fusion (Fig. 2d-f), we used the observation that *eff-1* is expressed also in P2.p cells, even though they already fused in the L1 larval stage, at a time similar to that observed in P3.p. Specifically, we found that animals with high *eff-1* expression in P3.p (>10 mRNA), always showed similar high levels in P2.p (data not shown). However, we also observed animals with high *eff-1* expression in P2.p, but low expression in P3.p (<5 mRNAs), which we interpreted as an animal where P3.p instead assumed VPC fate. Because of the observed variability in the time of fusion, body length was not useful to select for animals with P3.p close to fusion. However, when only selecting data for P3.p and P4.p cells in animals with high *eff-1* expression in P2.p (>10 mRNAs), we were able to increase the width of the peak, corresponding to high expressing cells in Figs. 2d-f.

## MODEL DETAILS

### Parameterization and fitting of BAR-1::GFP dynamics

To fit the experimentally measured BAR-1::GFP dynamics, we assume the following minimal model of BAR-1 production and degradation:

$$\frac{dc_{\text{BAR-1}}}{dt} = k_p - k_d \frac{1}{1 + \alpha S(t)} c_{\text{BAR-1}}, \quad (1)$$

where  $c_{\text{BAR-1}}$  is the BAR-1 level and  $k_p$  is the BAR-1 production rate. In the absence of Wnt signaling,  $S(t)=0$ , the degradation complex degrades BAR-1 at a basal rate  $k_d$ . However, in the presence of Wnt signaling,  $S(t)=1$ , the degradation complex is inhibited (Eisenmann 2005) and degradation occurs at a reduced rate  $\frac{k_d}{1+\alpha}$ , with  $\alpha > 1$ . In the model, we assume the BAR-1 pulse is generated by changes in Wnt signaling level  $S(t)$ . In particular, we assume Wnt signaling is activated at a constant level  $S(t)=1$  starting at time  $t_0$  and ending at time  $t_0+T$ , where  $T$  is the pulse duration. For other times, Wnt signaling is not activated,  $S(t)=0$ . These assumptions yield the following expression for the BAR-1 dynamics:

$$c_{\text{BAR-1}}(t) = \begin{cases} \frac{k_p}{k_d} & t < t_0 \\ \frac{k_p}{k_d} (1 + \alpha) - \alpha \frac{k_p}{k_d} e^{-k_d \frac{t-t_0}{1+\alpha}} & t_0 \leq t < t_0 + T \\ \frac{k_p}{k_d} + \alpha \frac{k_p}{k_d} \left(1 - e^{-k_d \frac{T}{1+\alpha}}\right) e^{-k_d(t-t_0-T)} & t_0 + T < t \end{cases} \quad (2)$$

For sufficiently long pulse duration  $T$ , the BAR-1 level will reach a steady state  $c_{\text{BAR-1}} = \frac{k_p}{k_d} (1 + \alpha)$ . However, in the experimentally obtained data we never observed BAR-1::GFP levels

reaching a steady state before the end of the pulse. Instead, we found that BAR-1::GFP accumulation remained approximately linear throughout the full duration of the pulse. Indeed, when the pulse duration is sufficiently short or the Wnt-mediated inhibition of BAR-1 degradation is sufficiently strong, i.e.  $(1 + \alpha) \gg k_d T$ , the exponential term in  $c_{\text{BAR-1}}(t)$  for  $t_0 \leq t < t_0 + T$  reduces to an expression that linearly with time in linear fashion, giving rise to the following expression used to fit the experimental data:

$$c_{\text{BAR-1}}(t) = \begin{cases} \frac{k_p}{k_d} & t < t_0 \\ \frac{k_p}{k_d} + k_p \frac{\alpha}{1 + \alpha} (t - t_0) & t_0 \leq t < t_0 + T \\ \frac{k_p}{k_d} + k_p \frac{\alpha}{1 + \alpha} T e^{-k_d(t-t_0-T)} & t_0 + T < t \end{cases} \quad (3)$$

We fitted this expression to the experimental BAR-1::GFP data by least-square fitting, using the implementation of the Levenberg-Marquardt algorithm, as implemented in the Python function `scipy.optimize.curve_fit` (Eric Jones *et al.* 2001) and using  $k_p$ ,  $k_d$ ,  $\alpha$ ,  $t_0$  and  $T$  as fit parameters. We obtained these fit parameters for each Pn.p cell by independent fitting. For fusing cells, we fitted  $c_{\text{BAR-1}}(t)$  to the experimental data only for time points until the experimentally determined time of fusion,  $t_{\text{fusion}}$ . We found that cell fusion always occurred before the end of the pulse, i.e.  $t_0 + T > t_{\text{fusion}}$  and, hence,  $T$  was not defined for fusing cells. In general, this fitting procedure provides good fits for most BAR-1::GFP trajectories, but fails to converge to a correct fit for trajectories with very low pulse amplitude or no apparent pulse. In that case, we assume  $c_{\text{BAR-1}}(t) = 0$ , with  $t_0$  and  $T$  not defined. To characterize pulse dynamics for non-fusing cell, we compare pulse onset time  $t_0$ , pulse duration  $T$  and pulse slope  $s = k_p \frac{\alpha}{1 + \alpha}$ . For fusing cells, pulse duration is not defined and instead we compare the time of fusion.

### Mathematical model of stochastic Pn.p cell fate decision

*Wnt signaling and eff-1 expression.* The model is briefly summarized in Fig. 6A,B of the main text. We assume that Wnt signaling (through BAR-1) and LIN-39 inhibit *eff-1* expression, whereas an activator A, whose identity is currently not known, induce *eff-1* expression. BAR-1 likely controls *eff-1* expression as a complex with the TCF/LEF transcription factor POP-1 (Korswagen *et al.* 2000). However, it is not known whether POP-1 and LIN-39 control *eff-1* expression in Pn.p cells by binding directly to the *eff-1* promoter, or whether they regulate the expression of other transcription factors that do. For simplicity, here we assume that these transcription factors bind directly and independently of each other to specific binding sites in the *eff-1* promoter and control *eff-1* expression in a combinatorial manner, with *eff-1* production only occurring when the activator A, but not LIN-39 and the BAR-1/POP-1 complex, are bound (Fig. 6A in the main text). Assuming that transcription factor (un)binding is rapid compared to *eff-1* expression dynamics, we have the following expression for *eff-1* level  $e$  in time:

$$e_i(t) = \left( \frac{K_W^n}{K_W^n + [c_{\text{BAR-1},i}(t)]^n} \right) \left( \frac{K_L^n}{K_L^n + c_{\text{LIN-39},i}^n} \right) \left( \frac{[c_{A,i}(t)]^n}{K_A^n + [c_{A,i}(t)]^n} \right), \quad (4)$$

where  $c_{\text{BAR-1},i}$ ,  $c_{\text{LIN-39},i}$  and  $c_A$  are the level of BAR-1, LIN-39 and the activator A in cell  $i$ ,  $n$  is a Hill coefficient and  $K_B$ ,  $K_L$  and  $K_A$  are the dissociation constants for the inhibition (BAR-1, LIN-39) and activation (A) of *eff-1* expression, respectively. Here, we assume that BAR-1 and activator levels vary in time but LIN-39 levels remain constant (based on Fig. 3 in the main text). Moreover, we assume that the level of the BAR-1/POP-1 complex scales linearly with  $c_{\text{BAR-1}}$ . To determine whether cell  $i$  assumes hyp7/fusion or VPC fate, we calculate the *eff-1* level  $e_i(t)$  as function of  $c_{\text{BAR-1},i}(t)$  and  $c_A(t)$  using Eq. 4. If  $e_i(t)$  is larger than a threshold value  $e_{\text{th}}$  for any given time  $t$ , cell  $i$  assumes hyp7/fusion rather than VPC fate. Based on the observed BAR-1 dynamics (Figs. 4 and 5 in the main text), we assume that the BAR-1 level increases linearly with slope  $s_i$  from the BAR-1 pulse onset time,  $t_0^i$ , onwards, with the level at time of fusion,  $t_f^i$  given by:

$$c_{\text{BAR-1},i}(t_f^i) = \begin{cases} s_i(t_f^i - t_0^i) & t_f^i > t_0^i \\ 0 & t_f^i \leq t_0^i \end{cases} \quad (5)$$

For the dynamics of the activator, we assume  $c_{A,i}(t)=0$  for  $t < t_f^i$  and a positive constant value  $c_{A,i}$  for  $t \geq t_f^i$ . We observe significant variability in the slope of the BAR-1 accumulation pulse (Fig. 5 in the main text). For that reason, we allow the pulse slope  $s_i$  in cell  $i$  to vary stochastically as:

$$s_i = \langle s \rangle + \eta_s^i, \quad (6)$$

where  $\langle s \rangle$  is the average slope and  $\eta_s^i$  is a white noise term that is intrinsic to cell  $i$ , i.e.  $\langle \eta_s^i \rangle = 0$  and  $\langle \eta_s^i \cdot \eta_s^j \rangle = \delta_{i,j}(\sigma_s)^2$  where  $\delta_{i,j}$  is the Kronecker delta and  $\sigma_s$  is the standard deviation of the noise. Similarly, we assume variability in the level of the activator A:

$$c_{A,i} = \langle c_A \rangle + \eta_A^i. \quad (7)$$

where  $\langle c_A \rangle$  is the average activator level at the time of fusion and  $\eta_A^i$  is a white noise source with  $\langle \eta_A^i \rangle = 0$  and  $\langle \eta_A^i \cdot \eta_A^j \rangle = \delta_{i,j}(\sigma_A)^2$ .

**Pulse and fusion timing.** We experimentally observed variability in pulse onset time and fusion time that can impact the inhibitory BAR-1 level at the time of fusion and, hence, control the frequency of hyp7/fusion versus VPC fate. We assume that the pulse onset time in cell  $i$  is given by:

$$t_0^i = \langle t_0 \rangle + \eta_0^c + \eta_0^i, \quad (8)$$

where  $\langle t_0 \rangle$  is the average observed pulse onset time,  $\eta_0^c$  is a white noise term common to all cells in an individual animal and  $\eta_0^i$  is a white noise term that is intrinsic to each cell  $i$ , i.e.  $\langle \eta_0^c \rangle = \langle \eta_0^i \rangle = 0$ ,  $\langle (\eta_0^c)^2 \rangle = (\sigma_0^c)^2$  and  $\langle \eta_0^i \cdot \eta_0^j \rangle = \delta_{i,j}(\sigma_0^{\text{int}})^2$ , with  $\sigma_0^c$  and  $\sigma_0^{\text{int}}$  the standard deviation of the common and intrinsic noise, respectively. For the cell fusion time, we assume:

$$t_f^i = \langle t_0 \rangle + \eta_0^c + \langle \Delta t_f \rangle + \eta_f^i, \quad (9)$$

where  $\langle \Delta t_f \rangle$  is the delay between the average pulse onset time and the average time of fusion and  $\eta_f^i$  is a cell-intrinsic white noise term with standard deviation  $\sigma_f$ . Equations 8 and 9 correspond to a picture where a common signal impacts the Pn.p cells at time  $t = \langle t_0 \rangle + \eta_0^c$  to

trigger both the start of the BAR-1 pulse and, after a delay  $\langle \Delta t_f \rangle$ , activation of cell fusion, but with added cell-intrinsic variability in the timing of both events.

**Constraining model by experiments.** We can constrain many of the model parameters using our experimental observations. For each mutant, we obtain the average pulse slope  $\langle s \rangle$  and standard deviation  $\sigma_s$  from the experimentally observed values, allowing us to approximate the experimental observation with a Gaussian distribution with mean  $\langle s \rangle$  and standard deviation  $\sigma_s$  (Supplemental Fig. 3a,b). We calculate mean pulse onset time as the average of the mean onset time in P3.p and P4.p,  $\langle t_0 \rangle = \frac{1}{2}(\langle t_0^3 \rangle + \langle t_0^4 \rangle)$ , i.e. the average of the mean pulse onset times observed in non-fusing P3.p and P4.p cells. For the variability in pulse onset time, we obtain estimates for the standard deviations  $\sigma_0^c$  and  $\sigma_0^{int}$  using the correlation function  $C_{i,j}^0 = \langle (t_0^i - \langle t_0^i \rangle)(t_0^j - \langle t_0^j \rangle) \rangle$ . In particular, we calculated the standard deviation of the common noise from the cross-correlation between the pulse onset in P3.p and P4.p,  $(\sigma_0^c)^2 = C_{3,4}^0$ . Next, using Eq. 8, we calculated the standard deviation of the cell-intrinsic noise as  $(\sigma_0^{int})^2 = \frac{1}{2}(C_{3,3}^0 + C_{4,4}^0 - 2C_{3,4}^0)$ . Using the estimated parameters, we obtained a good fit with the experimentally observed distribution of pulse onset time in P3.p (Supplemental Fig. 3c,d) and were able to reproduce the experimentally measured joint distribution of pulse onset time in P3.p and P4.p in Fig. 5e in the main text (Supplementary Fig. 3f). Fusing P3.p cells in the *bar-1(++);lin-39(lf)* mutant often exhibit a pulse with very low amplitude, making it challenging to determine the exact time of pulse onset. However, pulse onset is often strongly correlated between cells in the same animal. To measure the time between pulse onset and time of fusion, we therefore calculate the delay between the pulse onset in P4.p and time of fusion in P3.p, as  $\langle \Delta t_f \rangle = \langle t_f^3 - t_0^4 \rangle$ . To estimate the standard deviation  $\sigma_f$  we followed different strategies for the two mutant strains that exhibited Pn.p fusions, *bar-1(++);lin-39(0)* and *bar-1(++);cwn-1(0)*. For the *bar-1(++);lin-39(0)* strain, P3.p had a much higher fusion frequency than P4.p (Supplementary Table 1) and we only considered animals where P3.p assumed hyp7/fusion fate and P4.p assumed VPC fate. Here, using Eq. 9, we estimated the standard deviation in fusion time as  $(\sigma_f)^2 = C_{ff} - C_{f0}$ , where  $C_{ff} = \langle (t_f^3 - \langle t_f^3 \rangle)^2 \rangle$  and  $C_{f0} = \langle (t_f^3 - \langle t_f^3 \rangle)(t_0^4 - \langle t_0^4 \rangle) \rangle$ . For the *bar-1(++);cwn-1(0)* strain, P3.p and P4.p have similar, but low hyp7/fusion frequencies. Hence, we considered all animals where one cell, either P3.p or P4.p, assumed hyp7/fusion fate and the other assumed VPC fate. We estimated the standard deviation in fusion time as  $(\sigma_f)^2 = C_{ff} + C_{00} - 2C_{f0} - (\sigma_0^{int})^2$ , where  $C_{ff} = \langle (t_f - \langle t_f \rangle)^2 \rangle$ ,  $C_{00} = \langle (t_0 - \langle t_0 \rangle)^2 \rangle$  and  $C_{f0} = \langle (t_f - \langle t_f \rangle)(t_0 - \langle t_0 \rangle) \rangle$ . Here,  $\sigma_0^{int}$  is the standard deviation of the cell-intrinsic pulse onset noise as estimated from the pulse onset timing data. Using the estimated parameter values, the model reproduced the experimentally observed correlation between cell fusion time and BAR-1 pulse onset time (Supplemental Fig. 3g).

**Parameter values.** Even though we could estimate many model parameters directly from the experiments, this was not possible for all parameters. Because we did not observe cell fusions in the *bar-1(++)* strain, we were unable to measure the parameters  $\langle \Delta t_f \rangle$  and  $\sigma_f$  that dictate the timing of expression of the activator A. For that reason, we assumed that the value of these two

parameters was the same as for the *bar-1(++);lin-39(0)* strain. For the threshold *eff-1* level above which cell fusion occurs, we chose  $e_{th} = \frac{1}{2}$  and we assumed that *eff-1* induction occurred with Hill coefficient  $n=3$  for both inhibitors and the activator. The remaining parameters  $C_A$ ,  $\sigma_A$ ,  $K_A$ ,  $c_{LIN-39}$  and  $K_L$  were chosen so that the resulting frequency of hyp7/fusion fate matched the experimentally observed frequencies (Supplemental Table 1, Supplementary Fig. 3e), with the constraint that  $c_{LIN-39}=0$  for the *bar-1(++);lin-39(0)* strain. In addition to the simulations for the experimentally examined strains, we also simulated a hypothetical mutant that has the same hyp7/fusion frequency as the *bar-1(++);cwn-1(0)* mutant, but achieves this by reducing the BAR-1 pulse slope rather than the pulse onset time. For this hypothetical mutant, we used the same parameters as for the *bar-1(++)* strain, but lowered the average pulse slope  $\langle s \rangle$  until the desired hyp7/fusion frequency was found. For the *bar-1(++)* mutant, we were unable to find parameter combinations for which the hyp7/fusion frequency in the simulations was close to zero, as observed experimentally. This is likely because the fitted distribution of pulse slopes overestimates the number of cells with low pulse slope (Supplemental Fig. 3a) and, hence, low levels of inhibitory BAR-1. A complete list of all parameters is given in the table below:

Parameter	<i>bar-1(++)</i>	<i>bar-1(++); lin-39(0)</i>	<i>bar-1(++); cwn-1(0)</i>	Low pulse slope mutant	Parameter estimated from experiment
$\langle s \rangle$	0.33	0.27	0.31	0.20	Yes
$\sigma_s$	0.15	0.21	0.13	0.15	Yes
$\langle t_0 \rangle$	0.29	0.30	0.53	0.29	Yes
$\sigma_0^c$	0.051	0.095	0.121	0.051	Yes
$\sigma_0^{int}$	0.074	0.132	0.018	0.074	Yes
$K_B$	1.0	1.0	1.0	1.0	No
$\langle \Delta t_f \rangle$	0.21	0.21	0.11	0.21	Yes
$\sigma_f$	0.048	0.048	0.034	0.048	Yes
$\langle T_{L2} \rangle$	11.2	10.2	12.8	11.2	Yes
$\langle c_A \rangle / K_A$	1.3	1.3	1.3	1.3	No
$\sigma_A / K_A$	0.3	0.3	0.3	0.3	No
$c_{LIN-39} / K_L$	0.8	0.0	0.8	0.8	No
$e_{th}$	0.5	0.5	0.5	0.5	No
$n$	3	3	3	3	No

**Simulation.** For all simulations, we generated data for two cells, P3.p and P4.p, in  $1 \cdot 10^4$  animals. For each cell  $i$ , we generated stochastic values for  $s_i$ ,  $c_{A,i}$ ,  $t_0^i$  and  $t_f^i$  according to Eqs. 6-9, where we discarded pulse slope values  $s_i < 0$  as they are an artifact of fitting the experimental distribution by a Gaussian. Based on the values for pulse onset time and pulse slope, we calculated for each cell the inhibitory BAR-1 level  $c_{BAR-1}$  according to Eq. 5, the

resulting *eff-1* level according to Eq. 4 and marked each cell as hyp7/fusion rather than VPC fate if the *eff-1* level exceeded the threshold value  $e_{th}$ . In the above table, all times are expressed as fraction of larval stage duration. However, to facilitate comparison with the experimental distribution, the average pulse slope  $\langle s \rangle$  and its standard deviation  $\sigma_f$  are in units of fluorescence increase per hour. For that reason, when used the pulse slope to calculate the BAR-1 level  $c_{BAR-1}$  in the experimental units of fluorescence (Fig. 6h), we first converted the time between pulse onset and fusion from dimensionless units to hours, by multiplying the dimensionless time with the average L2 larval stage duration  $\langle T_{L2} \rangle$ .

## Acknowledgements

We thank Yvonne Goos and Joleen Traets for coupling *eff-1* primers to Cy5, and Yvonne Goos for minor technical assistance. We thank Renée van Amerongen, Rik Korswagen, Pieter Rein ten Wolde, and Tom Shimizu for helpful discussions on the manuscript. This work is part of the research program of the Netherlands Organisation for Scientific Research (NWO) and was performed at the research institute AMOLF. Some *C. elegans* strains were provided by the CGC, which is funded by NIH Office of Research Infrastructure Programs (P40 OD010440). The work was supported by a European Research Council Starting Grant (338200-STOCHCELLFATE) awarded to J.S.v.Z.

## Author Contributions

Conceptualization, J.S.v.Z.; Methodology, J.R.K. and J.S.v.Z.; Formal Analysis: J.R.K., J.T, and J.S.v.Z.; Investigation, J.R.K., and J.T.; Writing – Original Draft, J.R.K. and J.S.v.Z.; Writing – Review & Editing, J.R.K. and J.S.v.Z.; Funding Acquisition, J.S.v.Z.; Supervision, J.S.v.Z.

## Declaration of Interests

The authors declare no competing interests.

## References

- Alper S., Kenyon C., 2001 REF-1, a protein with two bHLH domains, alters the pattern of cell fusion in *C. elegans* by regulating Hox protein activity. *Development* 128: 1793–804.
- Alper S., Kenyon C., 2002 The zinc finger protein REF-2 functions with the Hox genes to inhibit cell fusion in the ventral epidermis of *C. elegans*. *Development* 129: 3335–3348.
- Balaban N. Q., 2004 Bacterial Persistence as a Phenotypic Switch. *Science*. 305: 1622–1625.
- Brabin C., Appleford P. J., Woollard A., 2011 The *Caenorhabditis elegans* GATA Factor ELT-1 Works through the Cell Proliferation Regulator BRO-1 and the Fusogen EFF-1 to Maintain the Seam Stem-Like Fate. *PLoS Genet.* 7: e1002200.
- Brenner S., 1974 THE GENETICS OF CAENORHABDITIS ELEGANS. *Genetics* 77: 71–94.
- Chen Z., Han M., 2001 *C. elegans* Rb NuRD and Ras regulate lin-39-mediated cell fusion during vulval fate specification. *Curr. Biol.* 11: 1874–1879.
- Clark S. G., Chisholm A. D., Horvitz H. R., 1993 Control of cell fates in the central body region of *C. elegans* by the homeobox gene lin-39. *Cell* 74: 43–55.
- Clevers H., Nusse R., 2012 Wnt/ $\beta$ -catenin signaling and disease. *Cell* 149: 1192–1205.
- Coudreuse D. Y. M., Giulietta R., Betist M. C., Destree O., Korswagen H. C., 2006 Wnt Gradient Formation Requires Retromer Function in Wnt-Producing Cells. *Science*. 312: 921–924.
- Edelstein A. D., Tsuchida M. A., Amodaj N., Pinkard H., Vale R. D., *et al.*, 2014 Advanced methods of microscope control using  $\mu$ Manager software. *J. Biol. Methods* 1: 10.
- Eisenmann D. M., Maloof J. N., Simske J. S., Kenyon C., Kim S. K., 1998 The beta-catenin homolog BAR-1 and LET-60 Ras coordinately regulate the Hox gene lin-39 during *Caenorhabditis elegans* vulval development. *Development* 125: 3667–3680.
- Eisenmann D. M., 2005 Wnt signaling. *WormBook*: 1–17.
- Eric Jones, Oliphant T., Peterson P., 2001 SciPy: Open Source Scientific Tools for Python. : <http://www.scipy.org/>.
- Félix M. A., 2012 *Caenorhabditis elegans* vulval cell fate patterning. *Phys. Biol.* 9.
- Gleason J. E., Korswagen H. C., Eisenmann D. M., 2002 Activation of Wnt signaling bypasses the requirement for RTK/Ras signaling during *C. elegans* vulval induction. *Genes Dev.* 16: 1281–90.
- Gleason J. E., Szyleyko E. a., Eisenmann D. M., 2006 Multiple redundant Wnt signaling components function in two processes during *C. elegans* vulval development. *Dev. Biol.* 298: 442–457.
- Goentoro L., Kirschner M. W., 2009 Evidence that Fold-Change, and Not Absolute Level, of  $\beta$ -Catenin Dictates Wnt Signaling. *Mol. Cell* 36: 872–884.
- Green J. L., Inoue T., Sternberg P. W., 2008 Opposing Wnt Pathways Orient Cell Polarity during Organogenesis. *Cell* 134: 646–656.
- Gritti N., Kienle S., Filina O., Zon J. S. van, 2016 Long-term time-lapse microscopy of *C. elegans* post-embryonic development. *Nat. Commun.* 7: 12500.
- Gupta B. P., Hanna-Rose W., Sternberg P. W., 2012 Morphogenesis of the vulva and the vulval-uterine connection\*. *WormBook*: 1–17.
- Harterink M., Kim D. H., Middelkoop T. C., Doan T. D., Oudenaarden A. van, *et al.*, 2011 Neuroblast migration along the anteroposterior axis of *C. elegans* is controlled by opposing gradients of Wnts and a secreted Frizzled-related protein. *Development* 138: 2915–2924.
- Hendriks G. J., Gaidatzis D., Aeschmann F., Großhans H., 2014 Extensive Oscillatory Gene Expression during *C. elegans* Larval Development. *Mol. Cell* 53: 380–392.
- Hill R. J., Sternberg P. W., 1993 Cell fate patterning during *C. elegans* vulval development. *Development* 18: 9–18.
- Hirabayashi Y., 2004 The Wnt/ $\beta$ -catenin pathway directs neuronal differentiation of cortical



- neural precursor cells. *Development* 131: 2791–2801.
- Hudson C., Kawai N., Negishi T., Yasuo H., 2013 B-Catenin-Driven Binary Fate Specification Segregates Germ Layers in Ascidian Embryos. *Curr. Biol.* 23: 491–495.
- Huelsz-Prince G., Zon J. S. van, 2017 Canalization of *C. elegans* Vulva Induction against Anatomical Variability. *Cell Syst.* 4: 219–230.e6.
- Jho E., Zhang T., Domon C., Joo C., Freund J., *et al.*, 2002 Wnt/ $\beta$ -Catenin/Tcf Signaling Induces the Transcription of Axin2, a Negative Regulator of the Signaling Pathway. *Mol. Cell. Biol.* 22: 1172–1183.
- Johnston R. J., Desplan C., 2010 Stochastic Mechanisms of Cell Fate Specification that Yield Random or Robust Outcomes. *Annu. Rev. Cell Dev. Biol.* 26: 689–719.
- Kafri P., Hasenson S. E., Kanter I., Sheinberger J., Kinor N., *et al.*, 2016 Quantifying  $\beta$ -catenin subcellular dynamics and cyclin D1 mRNA transcription during Wnt signaling in single living cells. *Elife* 5.
- Koh K., Peyrot S. M., Wood C. G., Wagmaister J. A., Maduro M. F., *et al.*, 2002 Cell fates and fusion in the *C. elegans* vulval primordium are regulated by the EGL-18 and ELT-6 GATA factors -- apparent direct targets of the LIN-39 Hox protein. *Development* 129: 5171–5180.
- Korswagen H. C., Herman M. a, Clevers H. C., 2000 Distinct beta-catenins mediate adhesion and signalling functions in *C. elegans*. *Nature* 406: 527–32.
- Korswagen H. C., 2002 Canonical and non-canonical Wnt signaling pathways in *Caenorhabditis elegans*: Variations on a common signaling theme. *BioEssays* 24: 801–810.
- la Cova C. de, Townley R., Regot S., Greenwald I., 2017 A Real-Time Biosensor for ERK Activity Reveals Signaling Dynamics during *C. elegans* Cell Fate Specification. *Dev. Cell* 42: 542–553.e4.
- Levine J. H., Lin Y., Elowitz M. B., 2013 Functional Roles of Pulsing. *Science*. 342: 1193–1200.
- Lindström N. O., Lawrence M. L., Burn S. F., Johansson J. A., Bakker E. R. M., *et al.*, 2014 Integrated  $\beta$ -catenin, BMP, PTEN, and Notch signalling patterns the nephron. *Elife* 3: e04000.
- Liu Z., Fujii T., Nukazuka A., Kurokawa R., Suzuki M., *et al.*, 2005 *C. elegans* PlexinA PLX-1 mediates a cell contact-dependent stop signal in vulval precursor cells. *Dev. Biol.* 282: 138–151.
- Losick R., Desplan C., 2008 Stochasticity and Cell Fate. *Science* 320: 65–68.
- Maamar H., Raj A., Dubnau D., 2007 Noise in Gene Expression Determines Cell Fate in *Bacillus subtilis*. *Science* 317: 526–529.
- Maloof J. N., Kenyon C., 1998 The Hox gene *lin-39* is required during *C. elegans* vulval induction to select the outcome of Ras signaling. *Development* 125: 181–90.
- Mentink R. A., Middelkoop T. C., Rella L., Ji N., Tang C. Y., *et al.*, 2014 Cell intrinsic modulation of Wnt signaling controls neuroblast migration in *C. elegans*. *Dev. Cell* 31: 188–201.
- Mila D., Calderon A., Baldwin A. T., Moore K. M., Watson M., *et al.*, 2015 Asymmetric Wnt pathway signaling facilitates stem cell-like divisions via the nonreceptor tyrosine kinase FRK-1 in *caenorhabditis elegans*. *Genetics* 201: 1047–1060.
- Mohler W. a, Shemer G., Campo J. J. del, Valansi C., Opoku-Serebuoh E., *et al.*, 2002 The type I membrane protein EFF-1 is essential for developmental cell fusion. *Dev. Cell* 2: 355–362.
- Mucenski M. L., Wert S. E., Nation J. M., Loudy D. E., Huelsken J., *et al.*, 2003  $\beta$ -Catenin Is Required for Specification of Proximal/Distal Cell Fate During Lung Morphogenesis. *J. Biol. Chem.* 278: 40231–40238.
- Myers T. R., Greenwald I., 2007 Wnt signal from multiple tissues and *lin-3*/EGF signal from the gonad maintain vulval precursor cell competence in *Caenorhabditis elegans*. *Proc. Natl. Acad. Sci. U. S. A.* 104: 20368–73.
- Ohyama T., 2006 Wnt signals mediate a fate decision between otic placode and epidermis. *Development* 133: 865–875.
- Park F. D., Priess J. R., 2003 Establishment of POP-1 asymmetry in early *C. elegans* embryos.

- Development 130: 3547–3556.
- Pénigault J. B., Félix M. A., 2011a Evolution of a system sensitive to stochastic noise: P3.p cell fate in *Caenorhabditis*. *Dev. Biol.* 357: 419–427.
- Pénigault J. B., Félix M. A., 2011b High sensitivity of *C. elegans* vulval precursor cells to the dose of posterior Wnts. *Dev. Biol.* 357: 428–438.
- Podbilewicz B., Leikina E., Sapir A., Valansi C., Suissa M., *et al.*, 2006 The *C. elegans* Developmental Fusogen EFF-1 Mediates Homotypic Fusion in Heterologous Cells and In Vivo. *Dev. Cell* 11: 471–481.
- Raj A., Bogaard P. van den, Rifkin S. A., Oudenaarden A. van, Tyagi S., 2008 Imaging individual mRNA molecules using multiple singly labeled probes. *Nat. Methods* 5: 877–879.
- Roiz D., Escobar-Restrepo J. M., Leu P., Hajnal A., 2016 The *C. elegans* hox gene *lin-39* controls cell cycle progression during vulval development. *Dev. Biol.* 418: 124–134.
- Roorda A., Williams D. R., 1999 The arrangement of the three cone classes in the living human eye. *Nature* 397: 520–522.
- Sarov M., Murray J. I., Schanze K., Pozniakowski A., Niu W., *et al.*, 2012 A Genome-Scale Resource for In Vivo Tag-Based Protein Function Exploration in *C. elegans*. *Cell* 150: 855–866.
- Sawa H., Korswagen H. C., 2013 Wnt signaling in *C. elegans*. *WormBook*: 1–30.
- Schindelin J., Arganda-Carreras I., Frise E., Kaynig V., Longair M., *et al.*, 2012 Fiji: An open-source platform for biological-image analysis. *Nat. Methods* 9: 676–682.
- Schneider C. A., Rasband W. S., Eliceiri K. W., 2012 NIH Image to ImageJ: 25 years of image analysis. *Nat. Methods* 9: 671–5.
- Shemer G., Podbilewicz B., 2002 LIN-39 / Hox triggers cell division and represses vulval cell fusion. *Genes Dev.* 16: 3136–3141.
- Shemer G., Suissa M., Kolotuev I., Nguyen K. C., Hall D. H., *et al.*, 2004 EFF-1 is sufficient to initiate and execute tissue-specific cell fusion in *C. elegans*. *Curr Biol* 14: 1587–1591.
- Shimojo H., Ohtsuka T., Kageyama R., 2008 Oscillations in Notch Signaling Regulate Maintenance of Neural Progenitors. *Neuron* 58: 52–64.
- Smallwood P. M., Wang Y., Nathans J., 2002 Role of a locus control region in the mutually exclusive expression of human red and green cone pigment genes. *Proc. Natl. Acad. Sci. U. S. A.* 99: 1008–1011.
- Smurova K., Podbilewicz B., 2016 RAB-5- and DYNAMIN-1-Mediated Endocytosis of EFF-1 Fusogen Controls Cell-Cell Fusion. *Cell Rep.* 14: 1517–1527.
- Sonnen K. F., Lauschke V. M., Uraji J., Falk H. J., Petersen Y., *et al.*, 2018 Modulation of Phase Shift between Wnt and Notch Signaling Oscillations Controls Mesoderm Segmentation. *Cell* 172: 1079–1081.e12.
- Sternberg P. W., Horvitz H. R., 1986 Pattern formation during vulval development in *C. elegans*. *Cell* 44: 761–772.
- Süel G. M., Garcia-Ojalvo J., Liberman L. M., Elowitz M. B., 2006 An excitable gene regulatory circuit induces transient cellular differentiation. *Nature* 440: 545–550.
- The *C. elegans* Deletion Mutant Consortium, 2012 Large-Scale Screening for Targeted Knockouts in the *Caenorhabditis elegans* Genome. *G3* 2: 1415–1425.
- Wang B. B., Müller-Immergluck M. M., Austin J., Robinson N. T., Chisholm A., *et al.*, 1993 A homeotic gene cluster patterns the anteroposterior body axis of *C. elegans*. *Cell* 74: 29–42.
- Zeev-Ben-Mordehai T., Vasishtan D., Siebert C. A., Grünwald K., 2014 The full-length cell-cell fusogen EFF-1 is monomeric and upright on the membrane. *Nat. Commun.* 5: 3912.
- Zernicka-Goetz M., Morris S. A., Bruce A. W., 2009 Making a firm decision: Multifaceted regulation of cell fate in the early mouse embryo. *Nat. Rev. Genet.* 10: 467–477.

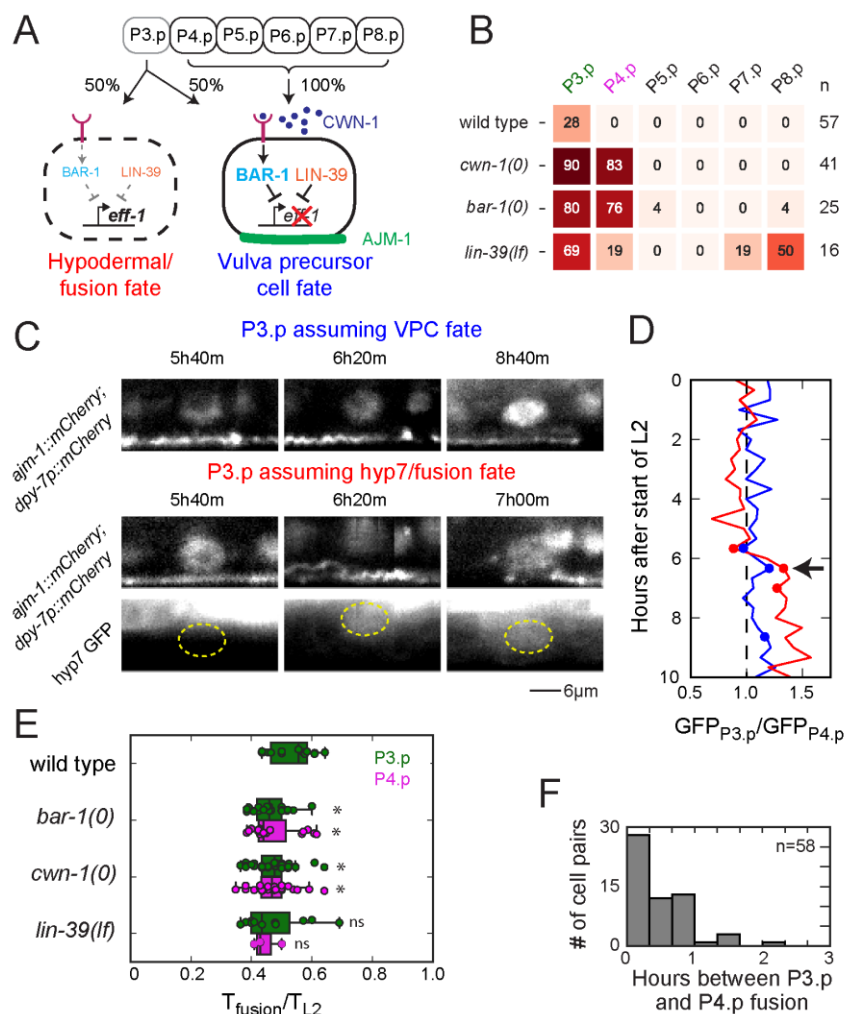


**Figure 1. Stochastic cell fate decisions in Pn.p cells.**

**(A)** Overview of the *hyp7/fusion* versus vulva precursor cell fate (VPC) decision in the P(3-8).p cells. Cells assuming *hyp7/fusion* fate fuse (indicated by the dashed line) with the hypodermal syncytium *hyp7* and lose the AJM-1 apical junction marker (green). Cell fusion requires the expression of the fusogen *eff-1* and is inhibited by the Hox protein LIN-39 and Wnt signaling through the  $\beta$ -catenin BAR-1. BAR-1 accumulation is induced by binding of Wnt ligands, such as CWN-1 (purple), to Wnt receptors (magenta). **(B)** Measured *hyp7/fusion* frequencies in Pn.p cells in wild-type and mutant backgrounds. Mutants carried the *ajm-1::gfp* reporter except for *lin-39(lf)* which carried *ajm-1::mCherry*. Wild-type animals carried either *ajm-1::gfp* (shown here) or *ajm-1::mCherry* (Supplemental Table 1), with no differences in fusion frequencies. **(C)** AJM-1 dynamics in non-fusing (top) and fusing (bottom) P3.p cells carrying a nuclear *dpy-7p::mCherry* marker. Cell fusion occurred 6h20m after the start of L2, as shown by the appearance of GFP from the hypodermal syncytium *hyp7* in P3.p (region enclosed by yellow line). Simultaneously, AJM-1 showed a pronounced ruffling, followed by its removal from P3.p. In contrast, no such AJM-1 dynamics was observed in non-fusing cells assuming VPC fate. **(D)** Comparing GFP inflow from the *hyp7* syncytium in fusing and non-fusing cells as a function of time after the start of the L2 larval stage. Shown is the ratio of GFP fluorescence intensity between P3.p and P4.p

in the same animal, where P4.p never fused. The blue and red line corresponds to the non-fusing and fusing cell in (C). Markers correspond to the time points shown in (C). Arrow indicates the time of AJM-1 ruffling and coincides exactly with inflow of GFP into the fusing cell. **(F)** Individual cell fusion times and box-and-whisker plots for P3.p (green) and P4.p cells (magenta) in different genetic backgrounds. Fusion time was determined for AJM-1 dynamics and is expressed as fraction of the L2 larval stage duration  $T_{L2}$  (~8hrs for all backgrounds). Even though small, but significant differences exist in average fusion time between strains (one-way ANOVA followed by Student's t-test, \* indicates  $P < 0.05$ ), the full distributions show extensive overlap. **(G)** Distribution of difference in cell fusion time between P3.p and P4.p cells, where both cells fuse (data pooled for all genotypes with double fusions).

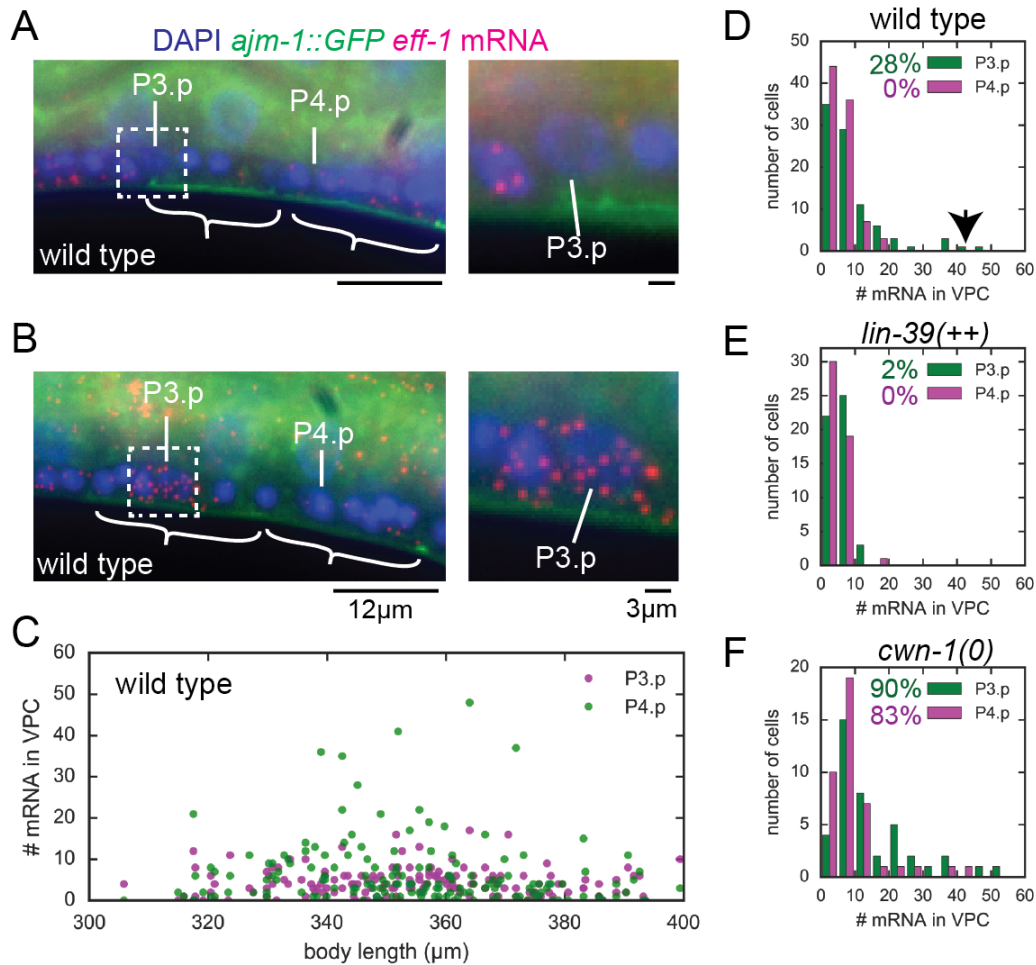


**Figure 2. Stochastic *eff-1* expression in Pn.p cells precedes cell fusion**

**(A),(B)** Example of (A) low and (B) high *eff-1* expression preceding cell fusion in wild-type animals of similar age, as determined by body length. Cells with high *eff-1* levels are expected to rapidly assume *hyp7*/fusion fate. Single *eff-1* mRNA molecules (red) were visualized using smFISH and nuclei with DAPI (blue). Unfused cells were selected based on *ajm-1::gfp* localization (green), with white brackets indicating intact apical junctions typical of unfused cells. Right-hand panels show details of the P3.p cell region, corresponding to the area delineated by the dashed line in the left-hand panels. **(C)** Number of *eff-1* spots in unfused cells as a function of developmental time, as measured by increasing body length. **(D), (E), (F)** Histograms of the distribution of the number of *eff-1* mRNAs in unfused P3.p and P4.p cells in (D) wild-type animals and mutants with (E) decreased or (F) increased *hyp7*/fusion frequency. We selected for animals with high *eff-1* expression in the P2.p cell to enrich for animals close to the time of fusion (see Methods for details). Whereas the distribution for low *eff-1* mRNA levels remains similar for the different strains, the fraction of animals showing high *eff-1* expression increases with increasing average *hyp7*/fusion fate frequency (as indicated for P(3,4).p).

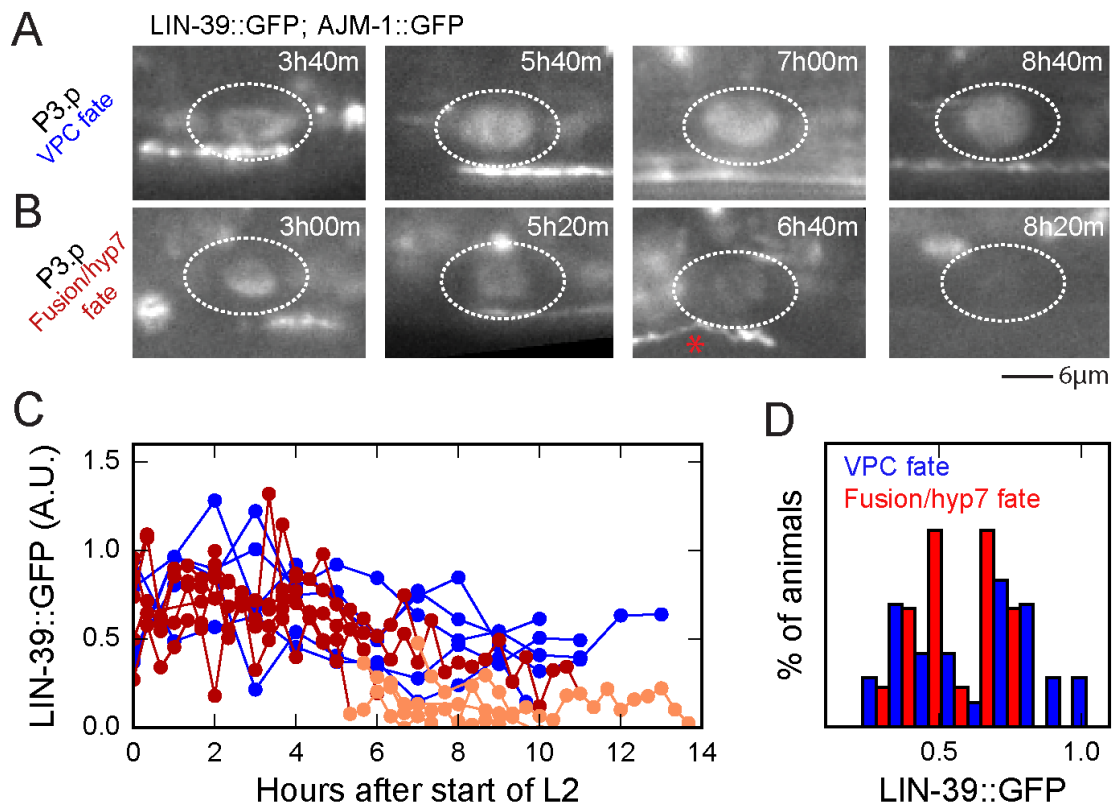
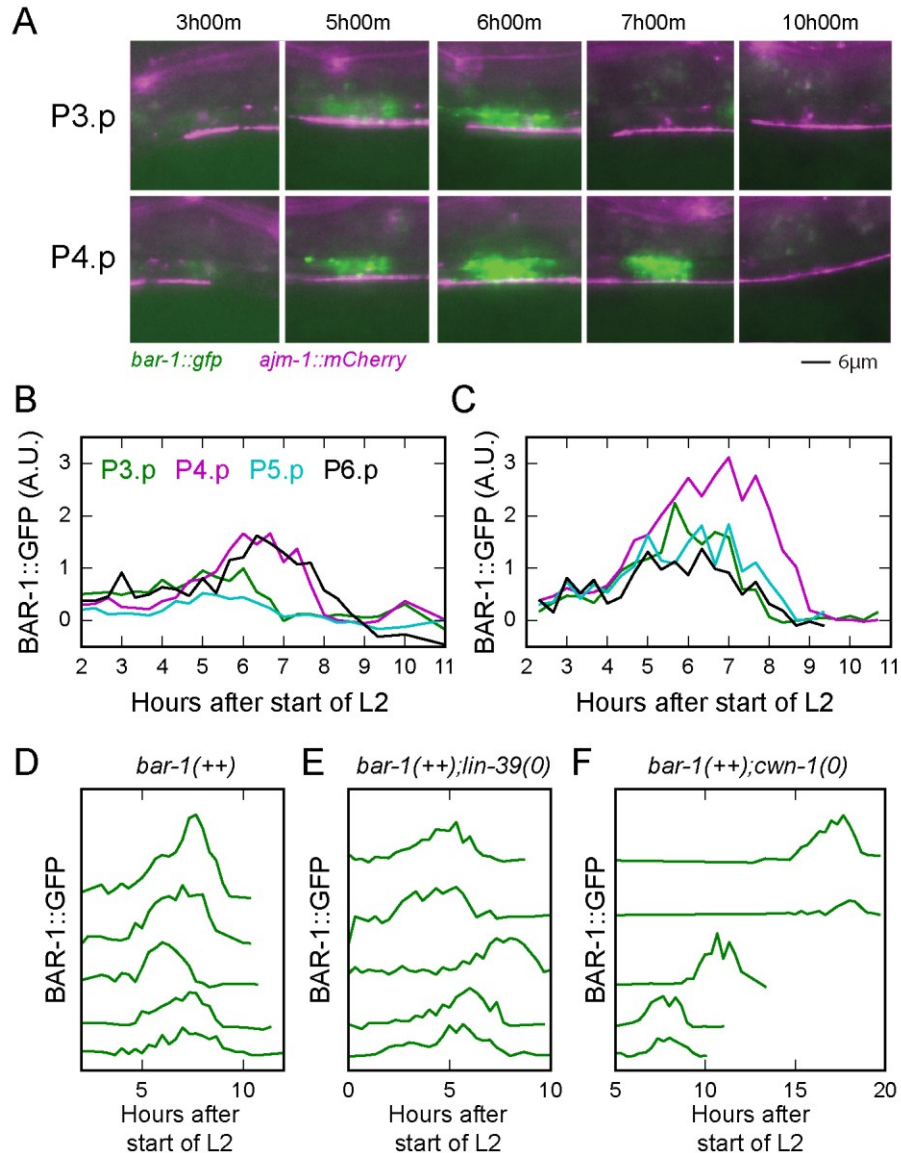


Figure 3. **Variability in LIN-39 protein level does not bias cell fate decision**

(A), (B) Image sequence of a cell assuming (A) VPC or (B) hyp7/fusion fate. Nuclear LIN-39 levels are visualized using a LIN-39::GFP protein fusion, while cell fusion is determined using an *ajm-1::GFP* reporter. The red star indicates cell fusion has occurred. Times are relative to the start of the L2 stage (C). Nuclear LIN-39 fluorescence in fusing (red) and non-fusing (blue) P3.p cells. For fusing P3.p cells, LIN-39 levels are variable prior to fusion (dark red) and fall rapidly after fusion (light red). (D) Distribution of nuclear LIN-39 fluorescence in fusing (red) and non-fusing (blue) P3.p cells show strong overlap. In fusing cells, fluorescence was averaged over 3 hour window directly prior to fusion, whereas in non-fusing cells a time window of 3 hours prior to the average time of cell fusion was used.



**Figure 4. Pulsatile BAR-1 dynamics during cell fate decision.**

**(A)** Image sequence of the BAR-1::GFP dynamics (green) over time in P3.p and P4.p cells in the same animal, with both cells assuming VPC fate. Animals also carry the *ajm-1::mCherry* marker (magenta). **(B),(C)** Dynamics of cellular BAR-1::GFP fluorescence in P(3-6).p cells in two different animals. The animal in (B) corresponds to images in (A). Different cells show similar timing of BAR-1 pulse onset, but vary in amplitude. **(D)-(F)** BAR-1::GFP dynamics in non-fusing P3.p cells in (D) *bar-1(++)*, (E) *bar-1(++);lin-39(0)*, (F) *bar-1(++);cwn-1(0)* animals. Traces for different animals are shifted along the vertical axis for clarity. Pulses show strong differences in time of onset and duration, even within the same strain. Traces run until the end of the L2 larval stage. Some *bar-1(++);cwn-1(0)* animals displayed significantly extended L2 stage duration (~15-20hr).

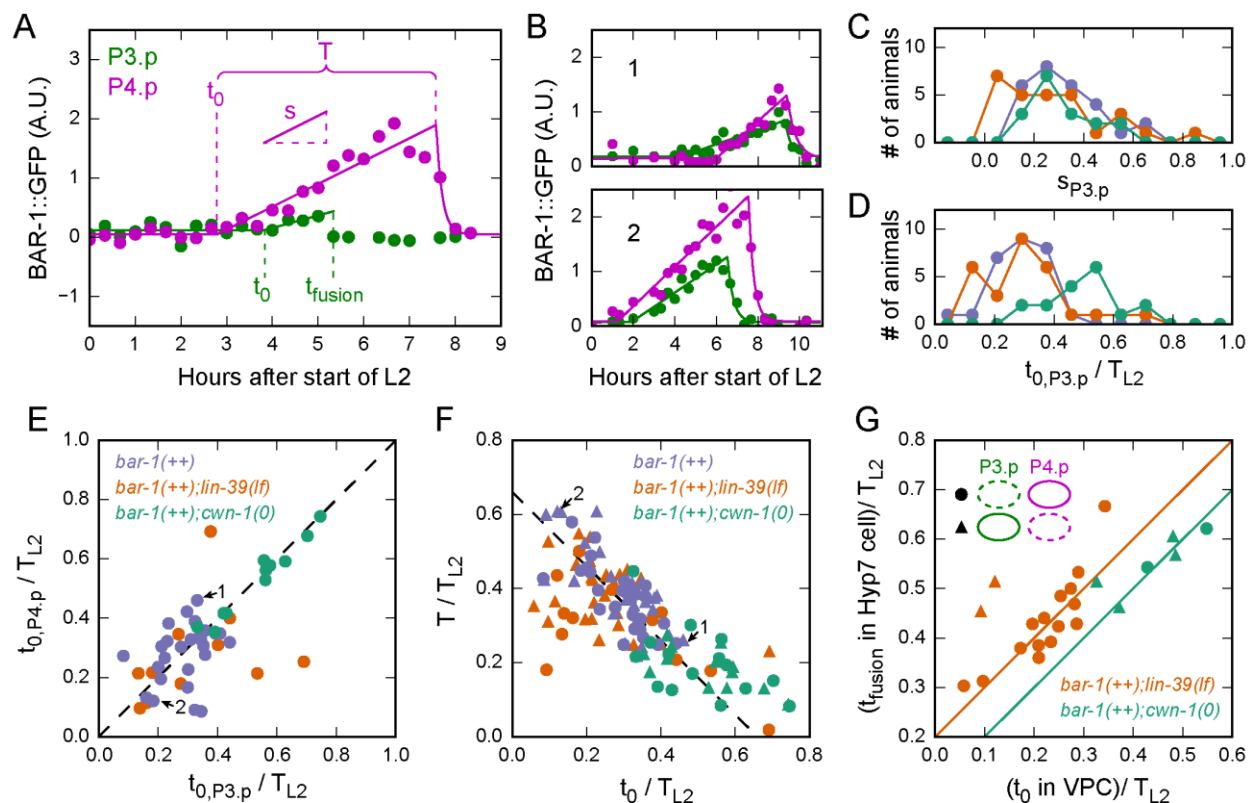


**Figure 5. Variability in BAR-1 pulse dynamics.**

**(A)** Quantifying BAR-1 pulse dynamics. Markers are measured BAR-1::GFP levels in P3.p (green) and P4.p (magenta). Here, P3.p, but not P4.p, assumed hyp7/fusion fate. Solid lines represent a model of BAR-1 accumulation dynamics (Eq. 3 in Methods). Using the model, each BAR-1 pulse is described by three key parameters: pulse onset time  $t_0$ , pulse slope  $s$  and pulse duration  $T$  (for non-fusing VPCs) or time of fusion  $t_{fusion}$  (for hyp7/fusion cells). **(B)** Animals showing differences in (relative) timing of BAR-1 accumulation pulses. **(C), (D)** Distribution of (C) pulse slope  $s$  and (D) pulse onset time  $t_0$  in P3.p cells, in  $bar-1(++)$  (purple),  $bar-1(++);lin-39(lf)$  (orange) and  $bar-1(++);cwn-1(0)$  mutants (green).  $T_{L2}$  is the L2 larval stage duration. Strains differ in BAR-1 pulse onset time rather than pulse slope. **(E)** Correlation in pulse onset time  $t_0$  between P3.p and P4.p cells. Each marker corresponds to a P3.p and P4.p cell in a single animal where both assumed VPC fate. Arrows indicate the animals in (B). **(F)** Correlation between pulse onset time  $t_0$  and pulse duration  $T$  in non-fusing P3.p (circles) and P4.p cells (triangles). The dashed line is  $T/T_{L2} = 0.66 - t_0/T_{L2}$ . BAR-1 pulses that start later in the L2 larval stage have a shorter duration. **(G)** Correlation between pulse onset time  $t_0$  in a VPC and fusion time  $t_{fusion}$  in a hyp7/fusion cell. Circles correspond to animals where P3.p, but not P4.p, assumed hyp7/fusion fate and triangles to animals where the cell fate assignment is reversed. The lines correspond to  $t_{fusion}/T_{L2} = \Delta T + t_0/T_{L2}$ , with  $\Delta T = 0.2$  (orange) and  $\Delta T = 0.1$  (green). The  $bar-1(++);cwn-1(0)$  mutant has a shorter time delay  $\Delta t$  between BAR-1 pulse onset and fusion.



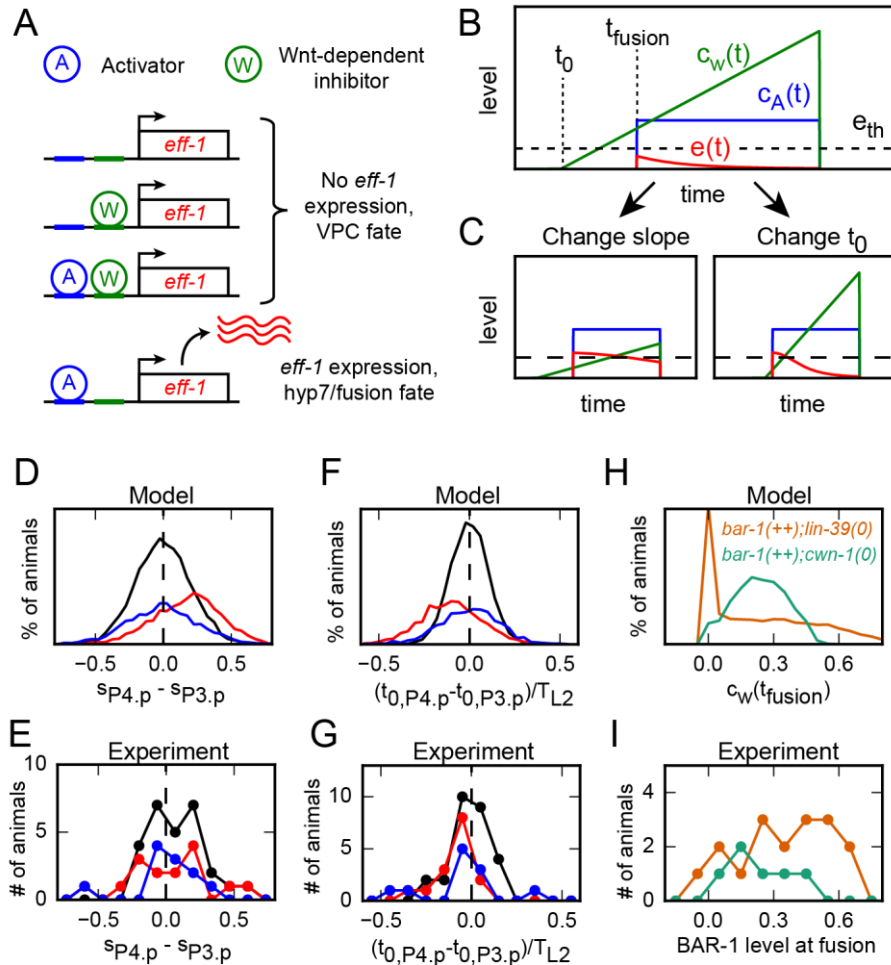


**Figure 6. Cell fate bias by variability in BAR-1 pulse timing.**

**(A)** Mathematical model of hyp7/fusion versus VPC fate decision. *eff-1* expression and, hence, hyp7/fusion fate is induced when the activator A, but neither BAR-1 (complexed with its co-activator TCF) nor LIN-39 is bound to the *eff-1* promoter. LIN-39 is not shown as its level is constant in time. **(B)** Temporal dynamics in the model. The *eff-1* expression level,  $e(t)$  (red) as function of the dynamic activation level  $c_A(t)$  (blue) and BAR-1 level  $c_{\text{BAR-1}}(t)$  (green), which increases linearly from pulse onset time  $t_0$ . Cell fusion is activated at time  $t_{\text{fusion}}$ , but only occurs for high activation  $c_A(t)$  and low inhibition  $c_{\text{BAR-1}}(t)$ , when *eff-1* is expressed above a threshold level  $e_{\text{th}}$  (dashed line). **(C)** In this model, fusion frequency can be changed both by changing the slope (left panel) and onset time (right panel) of BAR-1 pulses. **(D)**, **(E)** Distribution of the difference in pulse slope  $s$  for BAR-1 pulses in P3.p and P4.p, both for the (D) model and (E) experiments. Shown are distributions for *bar-1(++)* animals (black), where no Pn.p cells fuse, and *bar-1(++);lin-39(0)* animals where P3.p, but not P4.p, fused (blue) or where neither P3.p nor P4.p fused (red). Fusing P3.p cells have a bias towards low pulse slope. **(F)**, **(G)** Distribution of the difference in pulse onset time  $t_0$  for BAR-1 pulses in P3.p and P4.p, both for the (F) model and (G) experiments. Color indicates the same scenarios as in (D). Fusing P3.p cells tend to have a delayed pulse onset. **(H)**, **(I)** Comparing BAR-1 levels at the time of cell fusion between

*bar-1(++);lin-39(lf)* (orange) and *bar-1(++);cwn-1(0)* animals (green), both for the (H) model and (I) experiments. For the experiments, data for fusing P3.p and P4.p cells was pooled. The delayed BAR-1 pulse onset in *bar-1(++);cwn-1(0)* animals (Fig. 5g) caused lower BAR-1 levels at the time fusion was initiated.

## Supplemental Information

### Table S1

Genotype	Fusion rates (%) <sup>a</sup>						
	P3.p	P4.p	P5.p	P6.p	P7.p	P8.p	N
<i>ncls13[ajm-1::GFP]</i> <sup>b</sup>	28	0	0	0	0	0	<b>57</b>
<i>ouls20[ajm-1::mCherry]</i> <sup>b</sup>	37	0	0	0	0	0	<b>30</b>
<i>cwn-1(ok546);ncls13[ajm-1::GFP]</i> <b><i>cwn-1(0)</i></b>	90	83	0	0	0	0	<b>41</b>
<i>bar-1(ga80);ncls13[ajm-1::GFP]</i> <b><i>bar-1(0)</i></b>	80	76	4	0	0	4	<b>25</b>
<i>lin-39(gk893);ncls13[ajm-1::GFP]</i> <sup>c</sup> <b><i>lin-39(0)</i></b>	100	100	100	100	100	100	<b>17</b>
<i>lin-39(n709);ouls20[ajm-1::mCherry]</i> <b><i>lin-39(lf)</i></b>	69	19	0	0	19	50	<b>16</b>
<i>lin-39::GFP;HIS24-H2B::mCherry;</i> <i>ncls13[ajm-1::GFP]</i> <b><i>lin-39(++)</i></b>	2	0	0	0	0	0	<b>48</b>
<i>cwn-1(ok546);lin-39::GFP;HIS24-</i> <i>H2B::mCherry;ncls13[ajm-1::GFP]</i> <b><i>cwn-1(0); lin-39(++)</i></b>	20	14	1	0	0	0	<b>126</b>
<i>bar-1::GFP;ouls20[ajm-1::mCherry]</i> <b><i>bar-1(++)</i></b>	0	0	0	0	0	0	<b>30</b>
<i>bar-1::GFP;cwn-1(ok546);ouls20[ajm-</i> <i>1::mCherry]</i> <b><i>cwn-1(0); bar-1(++)</i></b>	6	8	0	0	0	0	<b>64</b>
<i>bar-1::GFP;lin-39(n709);ouls20 [ajm-</i> <i>1::mCherry]</i> <b><i>lin-39(lf); bar-1(++)</i></b>	24	4	3	0	13	19	<b>70</b>

Pn.p fusion frequencies in different genetic backgrounds with time-lapse microscopy techniques.

<sup>a</sup> Fusion rates are rounded to the nearest percentage. Fusion events were counted by the loss of *ajm-1* staining during the L2 stage, and non-fusion animals were only counted if the animal reached the L3 ecdysis without a fusion event.

<sup>b</sup> No statistical difference between P3.p fusion rates in these marker strains, (P= 0.47, Fisher's Exact Test).

<sup>c</sup> P3.p – P8.p fused prematurely in the L1 stage in the null mutant.

## Supplementary Figures

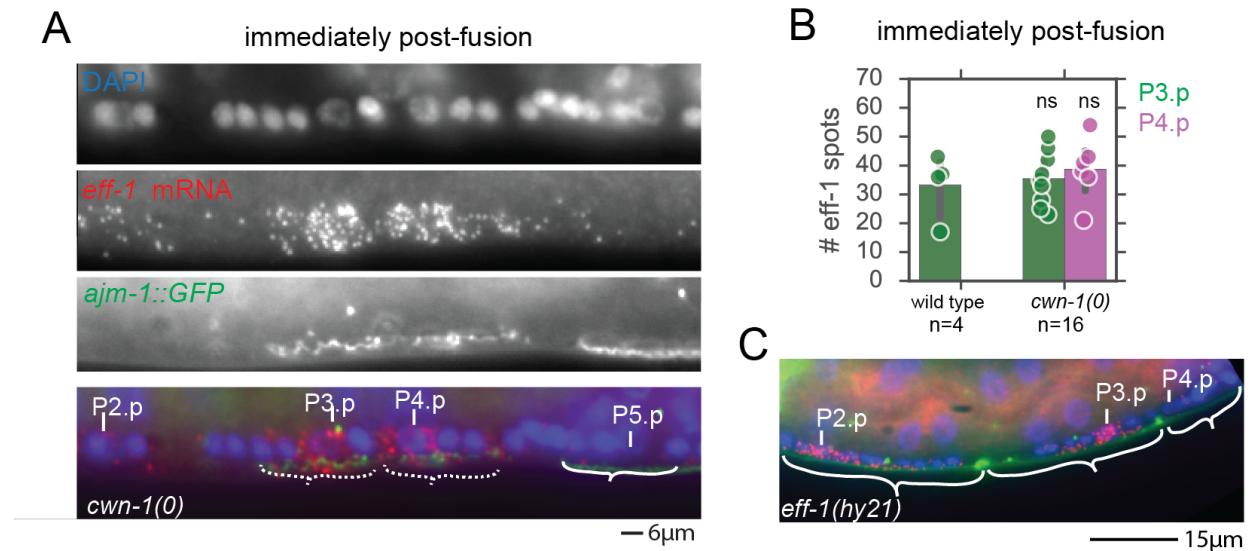


Figure S1. The gene *eff-1* is expressed at a high level before cell fusion.

**(A)** Example of an animal with both P3.p and P4.p showing evidence of recent fusion, due to the currently degrading and ruffled appeared of the *ajm-1::gfp* marked by dashed-white brackets. **(B)** Quantification of the number of *eff-1* spots in cells that have recently fused as in (A). Different genetic backgrounds show similar levels of *eff-1* expression at the time of fusion. Dots correspond to individual cells and are plotted with the average and standard error. No significant differences are present in the average number of *eff-1* spots. **(C)** Image of a mid-L2 stage *eff-1(hy21)* temperature-sensitive-mutant with a point mutation that renders the protein non-functional, but allows for mRNA staining with smFISH probes. High levels of *eff-1* expression are seen in P2.p and P3.p, despite them remaining unfused (marked by white brackets).

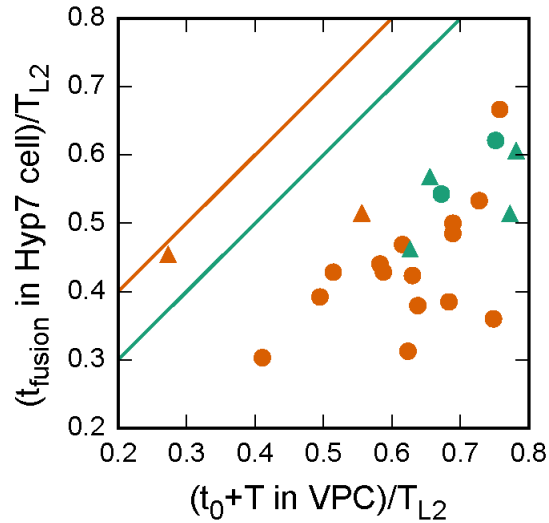


Figure S2. **Correlation between BAR-1 pulse end time and time of fusion**

Correlation between BAR-1 pulse end time  $t_0 + T$  in a VPC and fusion time  $t_{\text{fusion}}$  in a hyp7/fusion cell, where  $t_0$  is the pulse onset time and  $T$  the pulse duration. Circles correspond to animals where P3.p, but not P4.p, assumed hyp7/fusion fate and triangles to animals where the cell fate assignment is reversed. Color indicates the *bar-1(++)* (purple), *bar-1(++);lin-39(lf)* (orange) and *bar-1(++);cwn-1(0)* (green) mutants. The lines correspond to  $t_{\text{fusion}}/T_{L2} = \Delta T + t_0/T_{L2}$ , with  $\Delta T = 0.2$  (orange) and  $\Delta T = 0.1$  (green), and are the same as those in Fig. 5g in the main text. The correlation between pulse end time and time of fusion is weaker than that between pulse start time and time of fusion (Fig. 5g in the main text).

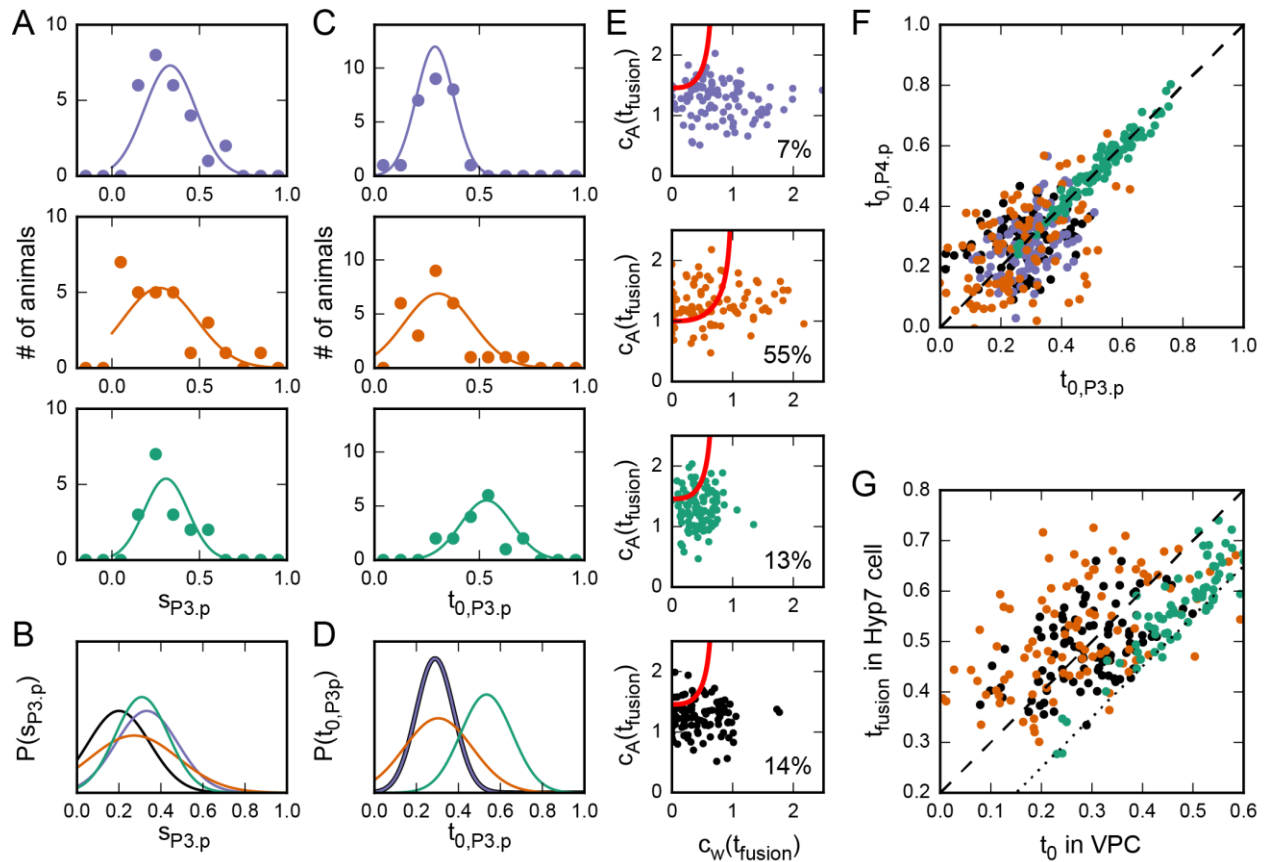


Figure S3. **Fitting minimal model to experimental observations.**

**(A)** Experimentally observed distribution of BAR-1 pulse slope  $s$  in the P3.p cell (markers) and the Gaussian fit used in the model (solid line). Color denotes the *bar-1(++)* (purple), *bar-1(++);lin-39(lf)* (orange) and *bar-1(++);cwn-1(0)* (green) mutants. **(B)** Comparison of pulse slope distributions in the model. Included are the distributions for the mutants in (A) and a hypothetical mutant with *hyp7/fusion* frequency similar to *bar-1(++);cwn-1(0)* but achieved by decreasing pulse slope rather than delaying pulse onset. **(C)** Experimentally observed distribution of BAR-1 pulse onset time  $t_0$  (markers) in the P3.p cell and the Gaussian fit (solid line). Color indicates the different mutant strains. **(D)** Comparison of pulse onset time between the different mutants. The distributions for the *bar-1(++)* (purple) and low pulse slope (black) mutants overlap. **(E)** Model simulations of cell fate decisions in the *bar-1(++)* (purple), *bar-1(++);lin-39(lf)* (orange), *bar-1(++);cwn-1(0)* (green) and low pulse slope (black) mutant. Each marker indicates the activator level  $c_A$  and inhibitory Wnt level  $c_W$  at the fusion time  $t_{\text{fusion}}$  for a single simulation. The red line indicates the boundary between activator and Wnt inhibition levels that result in *hyp7/fusion* fate (high  $c_A$ , low  $c_W$ ) or VPC fate (other). The lack of LIN-39 inhibition enlarges the *hyp7/fusion* region in the *bar-1(++);lin-39(lf)* mutant. For each mutant the *hyp7/fusion* frequency, calculated from  $1 \cdot 10^6$  simulations, is given. **(F)** Correlation between pulse onset time in the P3.p and P4.p cell in the same animal, generated by the model. Data is for the different mutants in (E). **(G)** Correlation between pulse onset time in P4.p and time of fusion in P3.p in animals where P3.p, but not P4.p, assumes *hyp7/fusion* fate. Color corresponds to the different mutants in (E). The lines correspond to  $t_{\text{fusion}}/T_{L2} = \Delta T + t_0/T_{L2}$ , with  $\Delta T=0.2$  (dashed line) and  $\Delta T=0.1$  (dotted line).

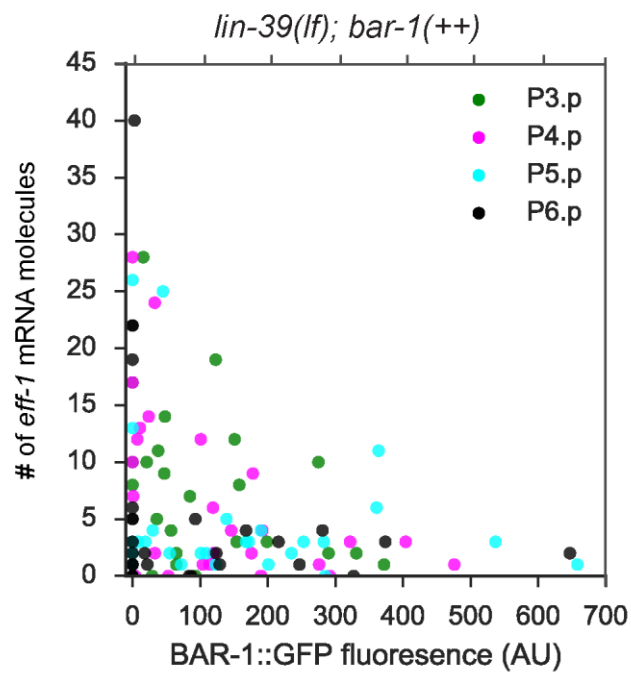


Figure S4. **Inverse relationship between *eff-1* expression and BAR-1::GFP levels.**

Number of *eff-1* mRNA molecules, as measured using smFISH, compared to the BAR-1::GFP fluorescence level in different Pn.p cells, with each marker corresponding to a single cell. BAR-1::GFP levels are permissive for high levels of *eff-1* expression, while high levels of BAR-1::GFP fluorescence block *eff-1* expression.

## Supplemental Methods Table 1

smFISH probes used to hybridize with *eff-1* mRNA molecules

Primer #	Probe (5'-> 3')
1	aactggggagaccactcaaa
2	gtaactgctaggagaagcag
3	ctcgagtggaaatccgtagg
4	ggaagagcccatcgaatttc
5	tgtcttggaacagtggtg
6	gagatgtttgagcacggaca
7	atctgaagcagactgcagtg
8	tcattgatctcttgggatgc
9	tccaaaagtgtaccgctgag
10	aactggcatgaacttcaggg
11	atgtggcatcacactcacag
12	agattctgcggtacatggtg
13	ctggacaagcggtaactga
14	gtttcatcagacttatcaga
15	gaacgtgcggtagcatgaag
16	cgattggtgtctgattggg
17	caaagcttgggatgctc
18	tggcttgaatcgaacgtcac
19	gactgcgaggaatgtcatat
20	acggttaggttgttctagt
21	gctgcgtagacaaatggtgc
22	tttatctttttocaccaat
23	tgtgttccaccatctaattg
24	cgacgtttttggtcgagatg
25	ggcagttacagccaatgaaa
26	cagttgatgagatgctcgtc

Primer #	Probe (5'-> 3')
27	ctccattacttgttcttgag
28	ttgcattctcagttctctg
29	attgtctgtaatctcattca
30	accatccaagacggtcaaag
31	atgaccagaatcgccattc
32	tcacaactccattattcaca
33	gccttgtgaatatcatccat
34	gctctttgcaatttttcact
35	acttcaagtggacgagtcaa
36	tcgagcagattgaatccacg
37	gtgttacaacagcttgtctg
38	tgaagattagttccttcggc
39	gacaaggttttgactttcca
40	agtcacgaattcttcatgca
41	tcaacgatgatggatccact
42	agcctcatatactgtcaagt
43	ctgatccatcaatttttcca
44	tccaaatccagttgacatct
45	gcagtgaaatgtggaattgt
46	cggtttgaagcatgaagatc
47	atggctggcagtggaataat



## Supplemental Movies

Movie S1: (Top panel) Apical junction marker AJM-1::mCherry and (bottom panel) GFP expressed in the hypodermal syncytium hyp7 for a P3.p cell assuming hyp7/fusion fate. At the time of fusion with hyp7, 6h20m after the start of the L2 larval stage, pronounced ruffling of AJM-1 is followed by its removal from P3.p. Concomitantly, GFP flows from the hyp7 syncytium into P3.p, as indicated by the yellow arrow. A *dpy-7p::mCherry* nuclear marker was used for cell identification (top panel).

Movie S2: (Top panel) Apical junction marker AJM-1::mCherry and (bottom panel) GFP expressed in the hypodermal syncytium hyp7 for a P3.p cell that assumes vulva precursor cell fate. AJM-1 is present in P3.p throughout the entire L2 larval stage and no inflow of GFP into P3.p is observed. A *dpy-7p::mCherry* nuclear marker was used for cell identification (top panel).

Movie S3: Pulsatile BAR-1 dynamics in P(3-5).p cells in a single animal. Time is relative to the start of the L2 larval stage. Each panel corresponds to a single cell. Shown are the apical junction marker AJM-1 (magenta) and BAR-1::GFP (green). The animal examined corresponds to that shown in Fig. 4a,b.